POLITECNICO DI MILANO

School of Industrial an Information Engineering

Master of Science in Mechanical Engineering

Design optimization of a Michelson Interferometer arm

Supervisor : Ing. Marco TARABINI

Co- Supervisor: Ing. Bortolino SAGGIN

Author:

Fernando Amaral Sarcinelli Garcia

10668221

Academic Year 2018 – 2019

Contents

1 Introduction 11
1.1 MIMA (Mars Infrared Mapper) 11
1.2 State of the art 19
1.2.1 Metal additive manufacturing in aerospace 19
1.2.2 Metal additive manufacturing technologies 23
1.2.3 Manufacturing and materials 24
1.2.4 Topology optimization 25
2 Methodology 30
2.1 Functional requirements and loading conditions 30
2.2 Design constraints 31
2.3 Materials 31
3 Single pendulum arm design 33
3.1 Introduction 33
3.2 Design constraints and optimization region 33
3.3 Choice of the best solution 34
3.4 FEA Model 37
3.4.1 Constraints and their equivalent on the FEA model (boundary conditions) 37
3.4.2 Mesh 40
3.4.3 Description of the static model (acceleration) 40
3.4.4 Description of the dynamic model (vibration modes) 41
3.5 Solutions analyzed 42
3.5.1 Previous model analysis 43
3.5.2 Honeycomb models 44
3.5.3 Material designer models 47
3.5.4 Topology optimization models 52
3.5.5 Lattice optimization models 57
3.5.6 External plate models 59
3.5.7 Comparison of the results and discussion 63
4 Double pendulum arm 70
4.1 Introduction 70

4.2 Design constraints and optimization region 70
4.3 FEA Model 72
4.3.1 Constraints and their equivalent on the FEA model (boundary conditions) 72
4.3.2 Mesh 73
4.4 Analysis 73
4.4.1 Analysis input 73
4.4.2 Initial results and further development 75
4.4.3 Further iterative optimization to find a suitable model. 76
4.5 Further required analysis 81
4.5.1 Fixation system compliance 81
4.5.2 Mirror displacement 85
5 Final discussion and conclusion 86

List of Tables

Table 1. Natural frequencies of the designed pendulum arm. 17
Table 2. Properties of the materials considered for this project's design 31
Table 3. Frequency coefficient variation according with the pendulum arm's first natural frequency value. 35
Table 4. Design coefficient variation according to the lattice element length. 36
Table 5. Analysis table of the previous pendulum arm model. 43
Table 6. Analysis table of the models developed with the honeycomb method. 45
Table 7. Analysis table of the best models developed with the honeycomb method. 46
Table 8. Analysis table of the models developed with the material designer method with diamond elements. 48
Table 9. Analysis table of the models developed with the material designer method with diamond with vertical bar elements. 49
Table 10. Analysis table of the models developed with the material designer method with diamond with external X elements. 49
Table 11. Analysis table of the models developed with the material designer method with diamond with central bar elements 50
Table 12. Analysis table of the best models developed with the ANSYS material designer method. 51
Table 13. Analysis table of the best models developed with the topology optimization method. . 57
Table 14. ANSYS lattice optimization input options. The minimum arm diameter is determined by the minimum density value. 58
Table 15. Analysis table of the first model developed with the external plate method. 61
Table 16. Analysis table of the best models developed with the external plate method. 62
Table 17. Analysis table of the best models overall and the previous design. 63
Table 18. Stress values for each mesh element size of the TO method stress convergence. 65
Table 19. Analysis table of the final model of the TO method. 66
Table 20. Stress values for each mesh element size e of the external plate method stress convergence. 68
Table 21. Analysis table of the final model of the external plate method. 69
Table 22. Natural frequencies of the final double pendulum design. 79
Table 23. Stress values for each mesh element size of the double pendulum stress convergence. 80
Table 24. Stress values for each mesh element size of the bolt force analysis stress convergence. 83

List of Figures

Figure 1. On the left a classic Michelson Interferometer, where one of the mirrors is stationary and the other moves linearly. On the right is the MIMA`s configuration, where a shaft rotates two mirrors at the same time thus having the same optical effect as the classic version but with much less space occupied. 12
Figure 2. MIMA Assembly. 13
Figure 3. Single pendulum arm with CCM attached. 14
Figure 4. Assembly of both pendulum arms, the CCMs and their fixing to the rotating shaft. 14
Figure 5. Pendulum arm final design. 15
Figure 6. Pendulum arm analysis, acceleration in the X axis, maximum stress of 73 MPa. 15
Figure 7. Pendulum arm analysis, acceleration in the Y axis, maximum stress of 108 MPa. 16
Figure 8. Pendulum arm analysis, acceleration in the Z axis, maximum stress of 70 MPa. 16
Figure 9. MIMA dynamic testing. 18
Figure 10. 3d printed turbine blade by SIEMENS. 19
Figure 11. Lattice test structures built on Renishaw AM250 metal AM system at The University of Nottingham, as part of the Aluminium Lightweight Structures via Additive Manufacturing (ALSAM) project. 20
Figure 12. Spyder bracket designed and built by Altair, Materialize and Renishaw. 21
Figure 13. Turbine designed and built by General Electric that uses many 3d printed components. 22
Figure 14. Representation of a powder-bed AM system. 23
Figure 15. Representation of a powder-fed AM system. 24
Figure 16. Initial model to be optimized. In green is the piece subject to the topology optimization analysis. 26
Figure 17. Raw results from the topology optimization. Needs post-processing. 27
Figure 18. Final results of the topology optimization, after the post-processing is finished. 27
Figure 19. Piece to be optimized using the level-set method. 28
Figure 20. Raw results of the level-set based optimization. 28
Figure 21. Different types of lattice elements. There are many more possible designs, these were given names by the author and will be further used in this project work. 29
Figure 22. Representation of the calculation procedure to reach the final acceleration input. 31
Figure 23. Comparison between the previous model and region selected to be kept unchanged on all analysis done. The transparent region is what was deleted from the previous model. 33
Figure 24. In orange is the optimizable region, the only part of the model that can be modified for the analysis done. 34
Figure 25. Evolution of the mass coefficient according to the pendulum arm`s total mass. 35
Figure 26. Graph of the frequency coefficient as a function of the first natural frequency of the pendulum arm. For high enough frequencies, it tends to 1. 36
Figure 27. Representation of the calculation procedure to reach the final design grade. 37
Figure 28. Pendulum arms and shaft assembly. In red, the region where the pendulum arms touch the shaft assembly. 38

Figure 29. In orange, region where pendulum arm touches the shaft assembly. This region has the Y displacement constrained and free X and Z displacement. 38
Figure 30. In orange, region where the bolt head is applying force. This region has the Y displacement constrained and free X and Z displacement. 38
Figure 31. In orange, region where the bolt body is located. This region has a cylindrical support with radial displacement constrained and free axial and tangential displacement. 39
Figure 32. Point mass in the model. The red surfaces are where the point mass is connected (they are rigid) and the sphere above them is the point mass location. 39
Figure 33. Surface mesh of the single pendulum model, with tetragonal elements. 40
Figure 34. Mode shape named by the author as lateral bending. 41
Figure 35. Mode shape named by the author as middle bending. 41
Figure 36. Mode shape named by the author as regular bending. 41
Figure 37. Mode shape named by the author as torsion. 42
Figure 38. Solidworks image of the previous pendulum arm model. 43
Figure 39. 6 mm length honeycomb. 44
Figure 40. 11 mm length honeycomb. 44
Figure 41. In orange are the changes done to ensure the stress is inside the threshold. On the left is for the 6 mm length honeycomb and on the right for the 11 mm length honeycomb. 46
Figure 42. Different types of lattice elements used in this project work. These were the only selected because they attend the 45° overhang constraint. Names were given by the author. 47
Figure 43. In orange is the region where the material designer equivalent material is applied. 48
Figure 44. True model of a pendulum arm filled with 3.33 mm diamond lattice elements. 50
Figure 45. Increase in lateral wall thickness to keep the maximum stress below the 203 MPa threshold. 51
Figure 46. Design region (blue) and exclusion region (red) used in the TO. 52
Figure 47. In orange is one of the symmetry planes inputted in the TO analysis. 53
Figure 48. In green is one of the symmetry planes inputted in the TO analysis. 53
Figure 49. TO results of the level-ser based analysis. 54
Figure 50. TO results of the density-based approach that has the goal of minimizing the mass while keeping the first natural frequency within a threshold. 55
Figure 51. TO results of the density-based approach that has the goal of maximizing the frequency while keeping the mass within a threshold. 55
Figure 52. First model developed with the TO analysis results. 56
Figure 53. X and Y dimensions were varied in order to find the values that yield the best design grade. 56
Figure 54. Lattice optimization done with diamond elements, 3.33 mm element size and minimum arm diameter of 0.5 mm. 58
Figure 55. Lattice optimization done with diamond elements, 3.33 mm element size and minimum arm diameter of 0.1 mm. Each image is one layer of the model. The three on the right indicate similar results as those obtained in the TO analysis. 59
Figure 56. Representation of polar moment of inertia calculation. The reference axis is the one in the center. 60

Figure 57. First design developed with the external plate method. Its section has the highest possible moment of inertia in all three axis. There is no upper plate because it would not be manufacturable by the AM process. 60
Figure 58. Design region (blue) and exclusion region (red) used in the TO for the external plate method. 61
Figure 59. External plate TO result. 62
Figure 60. Model generated by the result obtained in the TO. 62
Figure 61. Stress plot for the TO analysis model with refined mesh. 64
Figure 62. New model developed to reduce the maximum stress on the TO model. 64
Figure 63. Plot of the stress convergence fit (blue line) of the TO method. 65
Figure 64. Zoom of the region where the stress is maximum at the TO method analysis. 66
Figure 65. Final geometry of the model developed with the TO method. 66
Figure 66. Stress plot for the external plate model with refined mesh. 67
Figure 67. Final geometry of the model developed with the external plate method. 68
Figure 68. Plot of the stress convergence fit (blue line) of the external plate method. 69
Figure 69. Zoom of the region where the stress is maximum at the external plate method analysis. 69
Figure 70. Mirror (orange) + Pendulum Arms (yellow) +Shaft connection (cyan) + Shaft (grey). 70
Figure 71. Region to be optimized (grey) + Pendulum tips (yellow) + Mirror (orange). View 1. 71
Figure 72. Region to be optimized (grey) + Pendulum tips (yellow) + Mirror (orange). View 2. 71
Figure 73. Fixed support boundary condition (region in blue). 72
Figure 74. Two "point mass" are present (spheres A and B) and are connected to the surfaces where the pendulum tips has contact with the optimizable region (red surfaces). 72
Figure 75. Surface mesh on the double pendulum model. 73
Figure 76. Vertical symmetry constraint on the double pendulum model. 74
Figure 77. Horizontal symmetry constraint on the double pendulum model. 74
Figure 78. TO results for 10% of the original mass and maximum possible first natural frequency. 75
Figure 79. TO results for 15% of the original mass and maximum possible first natural frequency. 75
Figure 80. Initial double pendulum model developed with the TO results. 76
Figure 81. Iterative optimization of the initial shape. 1) Top-left; 2) Top-right; 3) Bottom-left; 4) Bottom-right. 76
Figure 82. Iterative optimization of the initial shape. 5) Top-left; 6) Top-right; 7) Bottom-left; 8) Bottom-right. 77
Figure 83. Iterative optimization of the initial shape. 9) Top-left; 10) Top-right; 11) Bottom-left; 12) Bottom-right. 77
Figure 84. Final optimized version of the double pendulum design. View 1. 78
Figure 85. Final optimized version of the double pendulum design. View 2. 78
Figure 86. Acceleration direction (+X +Z) that yields the highest stress on the part. 79
Figure 87. Plot of the stress convergence fit (blue line) of the double pendulum model analysis. 80

Figure 88. Zoom of the region where the stress is maximum at the double pendulum model analysis. 81
Figure 89. In orange on the left is the region where the shaft has contact with the double pendulum model. On the right is a representation of the torque and vertical forces measured at the ANSYS analysis. 82
Figure 90. ANSYS model to find the stress at the part when the bolts are tightened. 83
Figure 91. Plot of the stress convergence fit (blue line) of the bolt force analysis. 84
Figure 92. Stress plot at the bolt fixations when the bolt forces are applied. 84
Figure 93. Displacements input applied to the bolt fixations (yellow surfaces). 85

Abstract

In the 2006-2009 period, Politecnico di Milano and Agenzia Spaciale Italiana designed the MIMA (Mars Infrared Mapper), a spectrometer used to explore the Martian surface. It was intended to be attached to an automatic rover's mast and therefore, foresee harsh takeoff, landing and operating conditions. Due to the huge load and necessity to save weight, it was designed with the most advanced manufacturing processes and materials available.

Unfortunately, it was later decommissioned and never took part in any mission. Now, there is a request for a new design, keeping its same geometry but being lighter, for a posterior mission of similar kind.

Therefore, under the same statements as before, the manufacturing processes that yield the best strength/weight ratio and geometry flexibility must be used. Nowadays, this is metal Additive Manufacturing (AM), a fast-growing trend in the aerospace sector.

The scope of this thesis work is then to redesign one of the MIMA's parts, the pendulum arms, to have the minimum possible weight and to be produced by AM. Finite Element Analysis through ANSYS Mechanical is used for the dimensioning. For the choice of the materials, the most reliable commercially available materials are compared, being the stress relieved AlSi10Mg considered the most suitable for this design. Two different solutions to the problem were analyzed.

One consists of a single pendulum arm redesign and compares many different geometry design procedures to reach the final version. A 37% mass reduction is achieved, and the design that is considered the best is done by topology optimization of the base geometry.

The second merges both pendulum arms, making its assembly a single structure. This has many benefits, the main being the great reduction in the number of bolts and nuts required. It is designed only by topology optimization and the results show a mass reduction of 63% when compared with the mass of the pendulums assembly. However, it induces large displacements of the MIMA's mirrors when assembled, which makes this design, at its actual state, unable to fulfill all requirements.

Sommario

Tra il 2006 e il 2009 il Politecnico di Milano e l'Agenzia Spaziale Italiana hanno collaborato al design del MIMA (Mars Infrared Mapper), uno spettrometro utilizzato nell'analisi del suolo marziano. È stato progettato per essere agganciato ad un rover, deve quindi essere in grado di sopportare le fasi di decollo ed atterraggio, e condizioni di esercizio molto dure. A causa dei grandi carichi e del bisogno di pesare il meno possibile è stato progettato con materiali e tecnologie di ultima generazione.

Sfortunatamente il progetto è stato abbandonato in corso d'opera e lo spettrometro non è mai stato utilizzato. Oggi ci viene richiesto lo stesso spettrometro, conservandone la geometria ma ancora più leggero, da utilizzare in una missione simile a quella originale. Ci troviamo a dover utilizzare tecnologie che consentano il maggior rapporto resistenza-peso e grande flessibilità nella geometria. Oggi questa tecnologia è l'Additive Manufacturing (AM), in grande crescita nel settore aerospaziale.

Lo scopo di questa tesi è quello di riprogettare una parte specifica del MIMA, le "pendulum arms", minimizzandone il peso e utilizzando l'AM. Per il dimesionamento del pezzo abbiamo utilizzato il Metodo degli Elementi Finiti su ANSYS Mechanical. Per la scelta del materiale sono stati presi in considerazione quelli più affidabili. Viste le condizioni operative, la scelta è ricaduta sulla lega di Alluminio AlSi10Mg, che viene quindi considerato il più adatto al progetto. Sono state analizzate due diverse soluzioni al problema.

La prima consiste nella riprogettazione di uno dei due "pendulum arm". Sono stati comparati diversi metodi di progettazione per raggiungere la forma finale. Si è ottenuta una riduzione di peso di 37%, la tecnica migliore è una versione ottenutta con l'ottimizzazione topologica della geometria di base.

La seconda unisce i due bracci per creare una struttura unica. Questa geometria ha molti vantaggi, il più significativo è la diminuzione del numero di bulloni e viti necessari. Viene progettato utilizzando esclusivamente l'ottimizzazione topologica ed i risultati mostrano una riduzione del peso di 63% se comparata alla massa originale. Tuttavia questa soluzione genera un dislocamento non trascurabile degli specchi del MIMA, questa problematica rende la seconda geometria inadatta.

1 Introduction

1.1 MIMA (Mars Infrared Mapper)

The MIMA (Mars Infrared Mapper) is a Fourier transform interferometer (FTI), that works in the near-middle infrared region and was intended to be used on the Pasteur Instrument Payload for the ExoMars Rover mission [1] . This mission was issued by the European Space Agency (ESA) to investigate Mars' surface environment, with emphasis on its biology, being this payload the measurement instruments to accomplish this goal [2].

Its concept came from a previous design, the Planetary Fourier Spectrometer (PFS), a device used in the 2003 Mars Express Orbiter mission, also from the ESA [3]. This device made observations on atmospheric temperature and pressure. Its measurements are considered a big success, at 2004 it released the discovery of methane in the Mars atmosphere, implicating that an unidentified geological process or extremophile life form is active.

From all different instruments on the Pasteur payload, the MIMA is mainly responsible for mapping the mineralogical composition of the Martian surface and analyzing its atmosphere. It was designed to be mounted on an automatic rover's mast and, therefore, foresee harsh takeoff, landing and operating conditions. Because of this, the mass, volume, power consumption, thermal, and load constraints were very tight, challenging and required unusual solutions to be overcome [4].

Originally it was designed to be on the 2018 ExoMars mission, which was later postponed to 2022. However, both the 1kg version described on the next section and the miniaturized 250g version (later developed, called MicroMIMA [5]) were decommissioned from this launch, basically the first because it was too heavy and the second because it was too small. Thankfully, the ESA decided to reaccept the MIMA for a posterior mission, with the request of keeping the 1kg version profile but reducing mass wherever possible, using the best available manufacturing solutions. For this reason and to be competitive with similar instruments, the Italian Space Agency funded a research to investigate the benefits from the adoption of additive manufacturing techniques

The MIMA's mechanical parts were designed by the Politecnico di Milano (PoliMi) and the Agenzia Spaziale Italiana (ASI, Italian Space Agency) in 2006-2009 [4], [6], [7]. The constraints they worked with were given by the ESA and are as follows [1]:

- Maximum mass of 1 kg.
- Maximum dimensions of 140mm x 140mm x 120mm.
- Maximum power consumption of 7 W.
- Design load of 700 m/s² applied in any direction, due to the landing conditions.

- Non-operational temperature range of -90ºC to 120ºC, the lower because of the lack of power for thermal control on non-operative phase and the upper due to the possibility of being dry heat sterilized.
- Minimum first natural frequency of 140Hz to withstand takeoff and landing loads [8].

To accomplish these demanding design goals, unconventional solutions were adopted. The chosen optic configuration was of a double pendulum with cubic corner mirrors. This is a variation of the classic Michelson interferometer, more compact since there is no need for linear motion of mirrors, both are moved simultaneously by a shaft.

A sketch of the MIMA's optical layout is shown in Figure 1. The radiation is split at the beam splitter, reflects at both CCM (Cubic Corner Mirrors), remerges at the beam splitter now generating interference, and then is focused at the detector. The interference is generated because of the different distances traveled by each beam and can be controlled by rotating the shaft that connects to both CCMs, thus changing how much each of the separated beams travel [1].

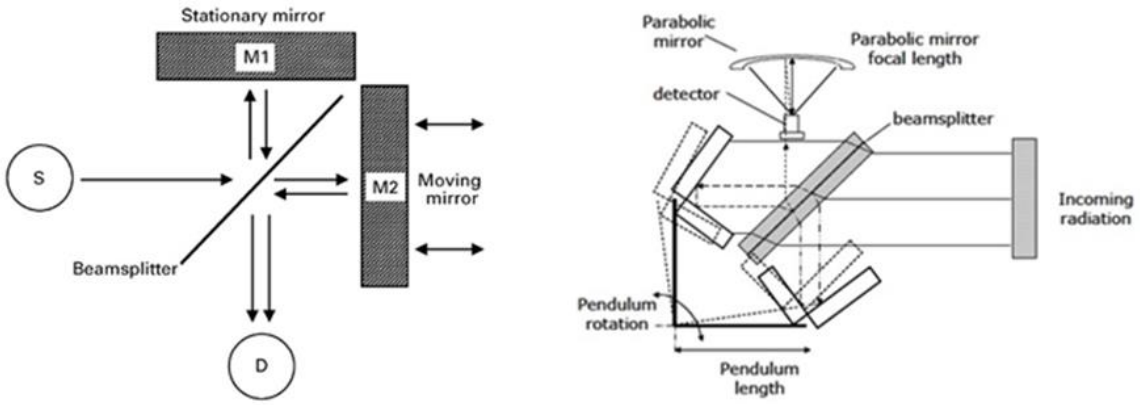

Figure 1. On the left a classic Michelson Interferometer, where one of the mirrors is stationary and the other moves linearly. On the right is the MIMA`s configuration, where a shaft rotates two mirrors at the same time thus having the same optical effect as the classic version but with much less space occupied.

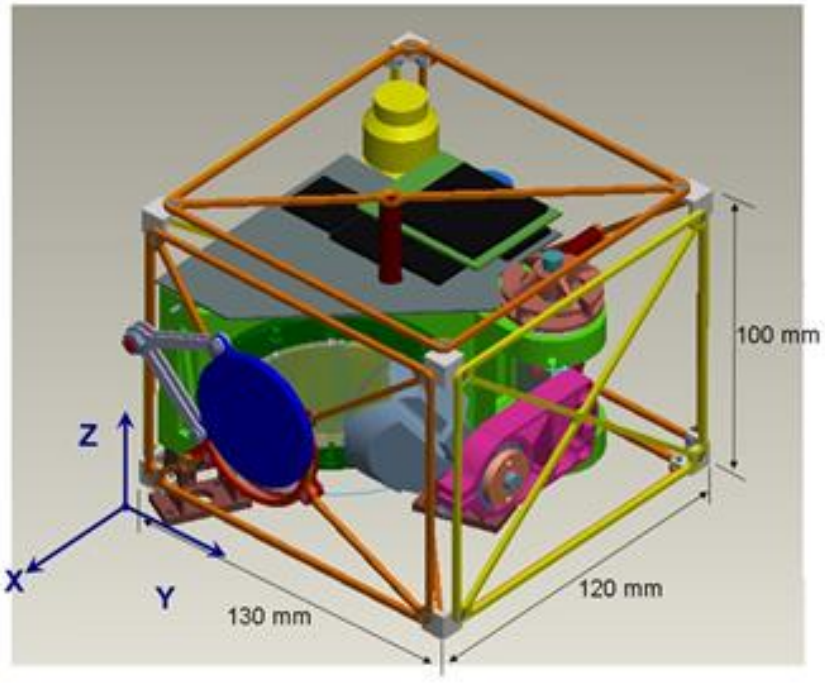

Figure 2. MIMA Assembly.

After the definition of the mirror configuration, all mechanical parts were designed. The subassemblies optical bench (OB), double pendulum (DP), beam splitter assembly (BA) and external box (EB) were each analyzed separately by Finite Element Analysis (FEA) models. The design of all components is detailed at [4], [6], [7], here, emphasis will be given to the DP, which will be the scope of this thesis work. This subassembly alone had 198 g, almost 20% of the maximum allowable mass [6].

This specific part in pink on Figure 3 and Figure 4 is called “pendulum arm”. It has the main purpose of connecting the CCM to the rotating shaft while allowing proper alignment of it. In the field of work of low wavelength optics (the MIMA measures in the 5-25 μm spectral range [7]), even a 1 μm misalignment can cause measurement issues. Thus, the three bolt holes have diameters higher than those of the bolts to allow for some displacement when its being aligned and the mirror has an alignment spherical joint to allow for rotation freedom.

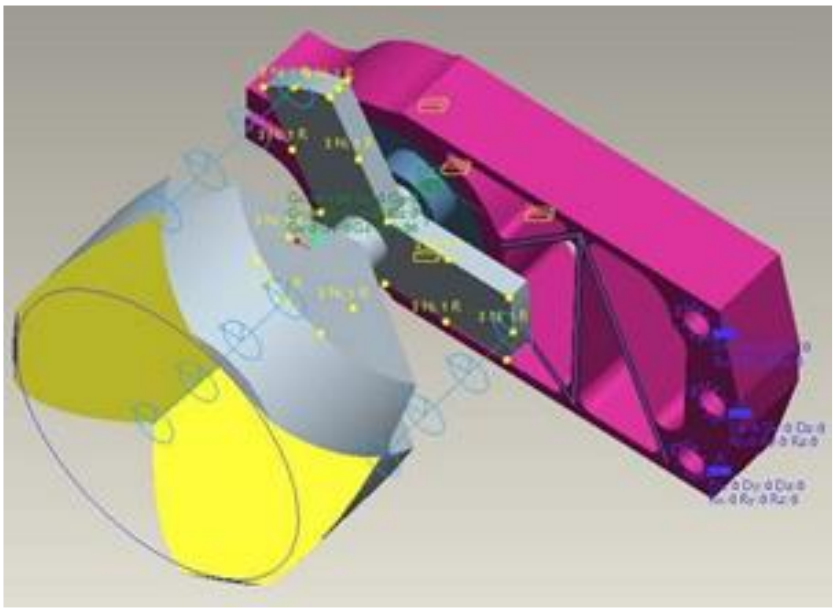

Figure 3. Single pendulum arm with CCM attached.

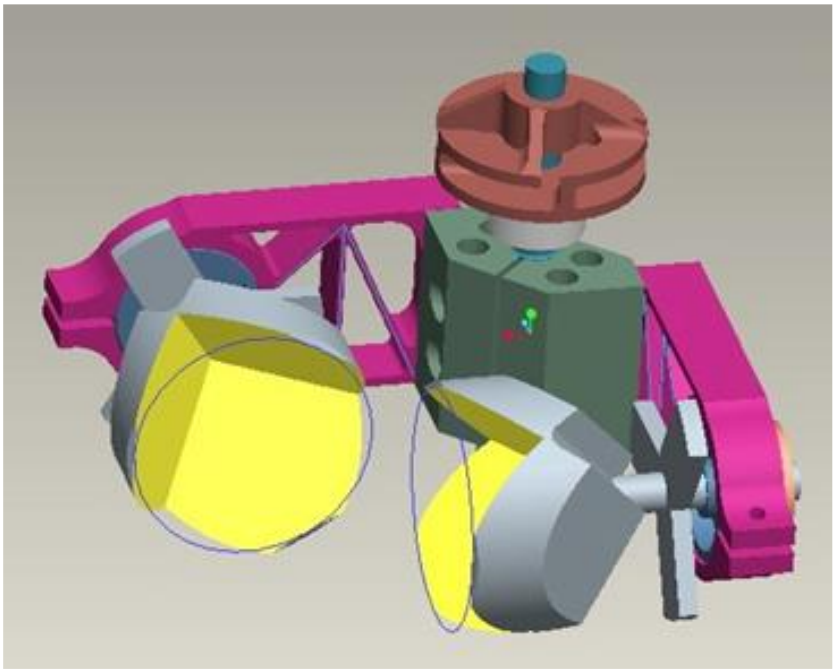

Figure 4. Assembly of both pendulum arms, the CCMs and their fixing to the rotating shaft.

As can be seen on Figure 3, there were used fixed supports (all 6 dofs constrained) on the bolt holes and the CCM was inserted on the system to have its mass affecting the acceleration static analysis. The chosen material of this part and most other parts was Al-7075-T6 so thermal contractions mismatch are avoided [6]. The result is Figure 5, obtained after multiple design iterations. The results of the static and dynamic analysis of this geometry are below. The thermal

analysis and testing were not critical on the DP subassembly because it is not a static indeterminate component and all other components it is connected to are made of the same material.

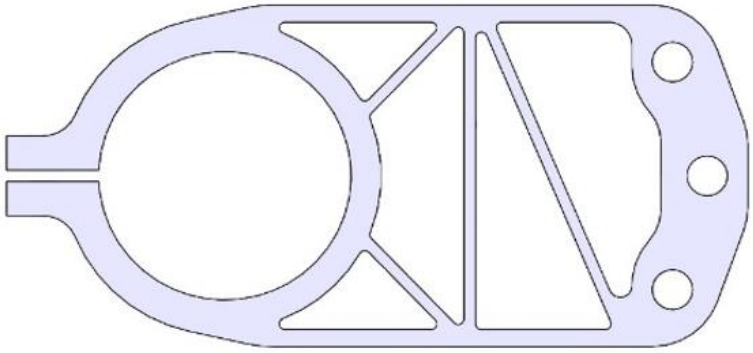

Figure 5. Pendulum arm final design.

For the static analysis, a load of 1000 m/s² was applied on the three main axis, having the maximum value of the three considered the design case. The maximum was obtained in the Y direction, of 108 MPa, resulting in a safety factor of 4.

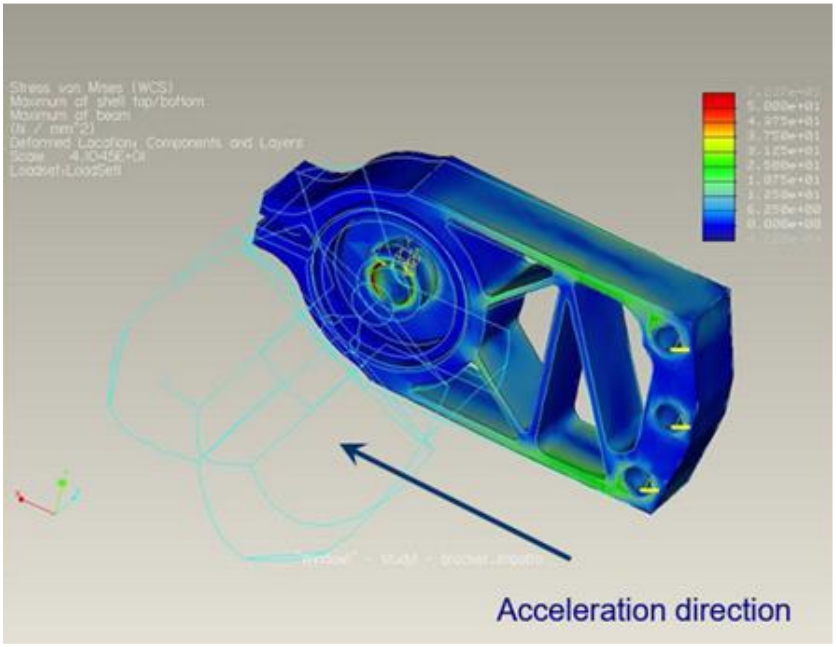

Figure 6. Pendulum arm analysis, acceleration in the X axis, maximum stress of 73 MPa.

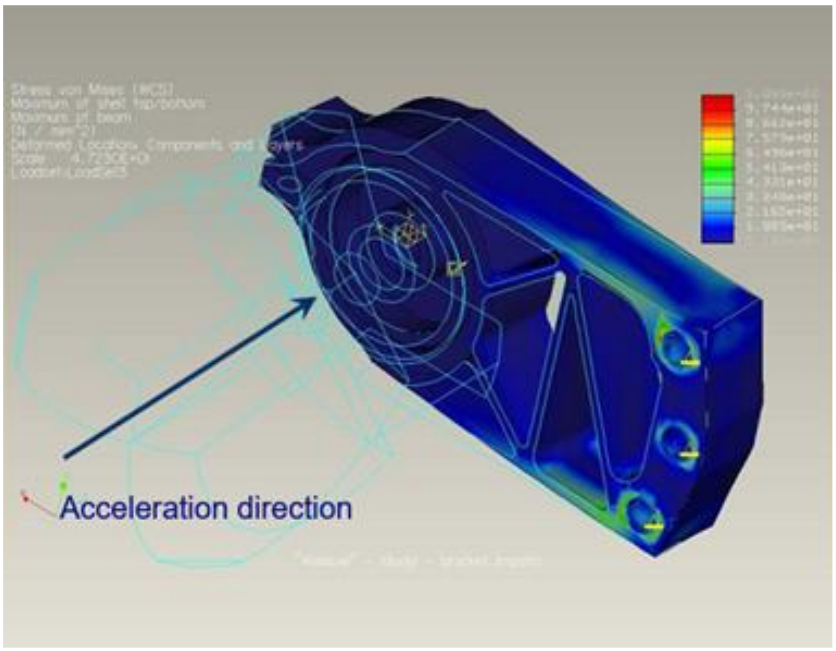

Figure 7. Pendulum arm analysis, acceleration in the Y axis, maximum stress of 108 MPa.

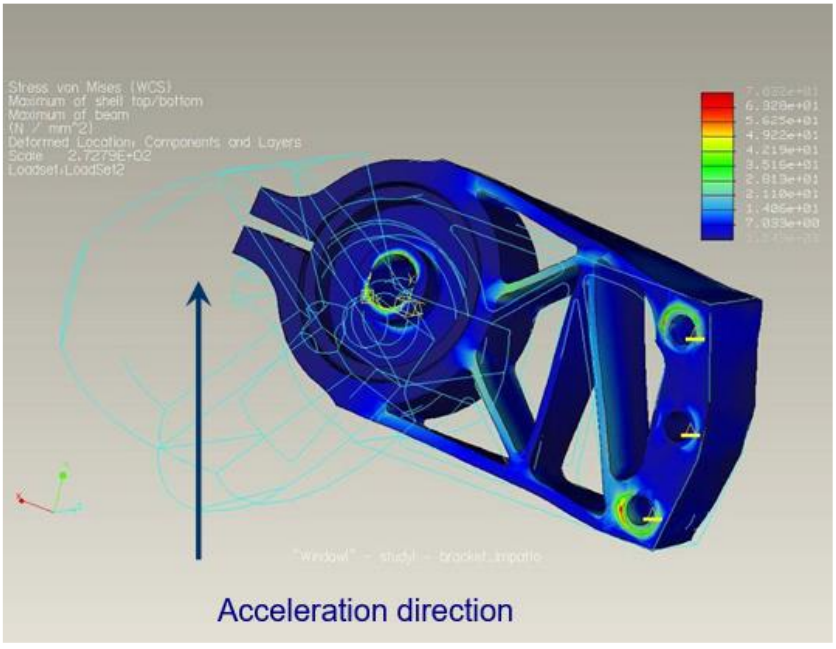

Figure 8. Pendulum arm analysis, acceleration in the Z axis, maximum stress of 70 MPa.

For the dynamic case, a simple modal analysis was done with the same boundary conditions as the static analysis. The results are displayed in Table 1.

Mode #	Frequency
1	390 Hz
2	540 Hz
3	910 Hz
4	980 Hz

Table 1. Natural frequencies of the designed pendulum arm.

This model was manufactured with Electro Discharge Machining (EDM) to be compliant with the very strict tolerance requirements. The resulting weight of was of 14.60 g. After the FEA, experimental testing was done to verify the design.

Since no thermal analyses are done, the only experimental tests required were for the launch vibrations and the acceleration shock. The latter was not done because no facility was available at the time.

For the dynamic testing, the whole assembled MIMA model was mounted on the head of an electro-dynamic shaker, instrumented with accelerometers, and tested according to the ESA guidelines [9]. Therefore, four different approaches were used, on all three reference axis of Figure 2: sweep sine test in the 20-2000 Hz range with very low acceleration amplitude (5 ms^{-2}), a sweep sine on the 10-100 Hz range with constant acceleration amplitude of 200 ms^{-2}, a random excitation on the 20-2000 Hz range for 2.5 minutes and RMS of 140 ms^{-2} and a shock test, with the maximum shock achievable by the shaker applied to the instrument. These tests detected no significant amplification on the 0-150 Hz range, thus validating the model.

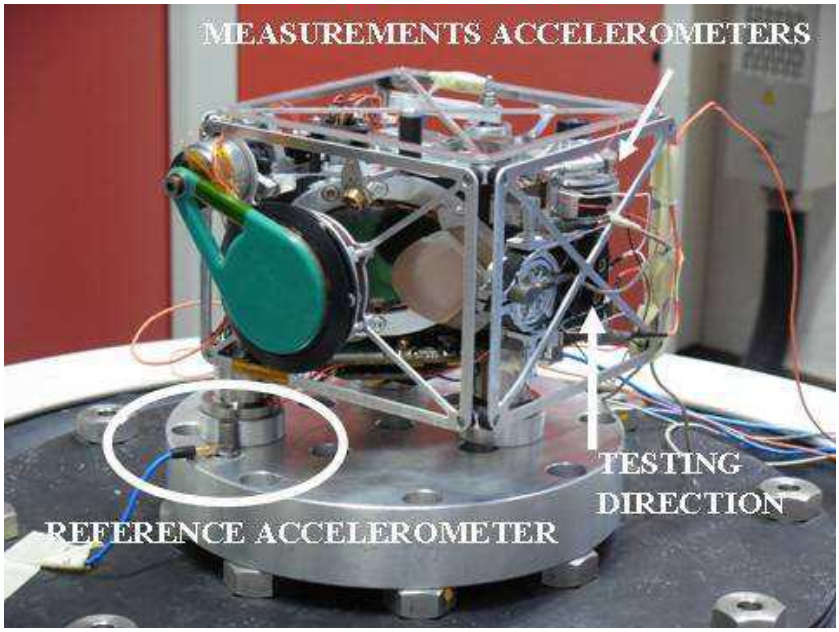

Figure 9. MIMA dynamic testing.

Comparing the time when the MIMA was initially designed and nowadays, the main turnaround in aerospace manufacturing was the addition of 3d printed parts. In summary, it radically changes the design possibilities because it works in a buildup procedure, adding material where it is required instead of removing, thus being contrary to what is done in the machining processes.

Then, multiple parts that were previously manufactured and then assembled now can be done in a single item. Complexity, a very costly parameter in regular machining, in AM, has no extra price on material, cost and sometimes not even on time. The possibility to have complex structures at no extra expense and with good tolerances is a strong positive point for the adoption of this on the MIMA design.

Consequently, this work will analyze many different design approaches that make use of the AM capabilities with the aim of reducing mass while keeping a safety margin on the design parameters. It will be organized by the presentation of the state of the art for current AM design and manufacturing, the methodology which leads to the FEA optimization of both a single arm of the DP and, of the whole DP assembly as a single piece.

1.2 State of the art

1.2.1 Metal additive manufacturing in aerospace

The aerospace sector is always in constant need for lightweight components to improve fuel efficiency and reduce emissions while keeping safety and reliability [10], [11]. Focus on lightweight design results in huge cost savings from the beginning to the end of a system's life [12]. To achieve this goal, the main request is design freedom, being able to manufacture the optimal solution in every case [13]. For this, metal AM has many different tools and capabilities which allows it to fit perfectly in this sector.

Firstly, lightweight structures requests material to be only where it is necessary. Because AM processes build components layer by layer, there can be empty spaces wherever mass is not required, contrary to the traditional machining processes which, as an example, cannot produce hollow singular parts. A successful case study is Siemens' 3d printed turbine blades, fully validated under regular loading conditions. The internal structure's complex shape greatly improves cooling while reducing mass. It was also reported that the lead time devoted to prototype development was reduced by 90% comparing with traditional processes [14].

Figure 10. 3d printed turbine blade by SIEMENS.

Moreover, AM parts have highly increased functional complexity. This is when a single piece can integrate multiple functions, many not traditionally assigned to it. A load-bearing component, for example, can also be a heat dissipator, electrical conduit and have flexible behavior [10]. Figure 10 shows a good example, adding a cooling function to the turbine blade.

Another successful example are lattice structures which occupy a part's internal areas to generate very high strength-weight ratios [15] . They allow for the solid material to be exactly where it has more impact on the component stiffness (usually the outer walls), while maintaining structural integrity by filling the inside. An interesting case study is the spider bracket design in Figure 12, a very organic structure made of lattice and fully solid regions. It was optimized to have solid material where it is structurally required and a thin lattice elsewhere, so the best possible load paths are achieved. Since building a complex part does not have an impact on the price at AM [16], the complex's structures advantages can be fully exploited.

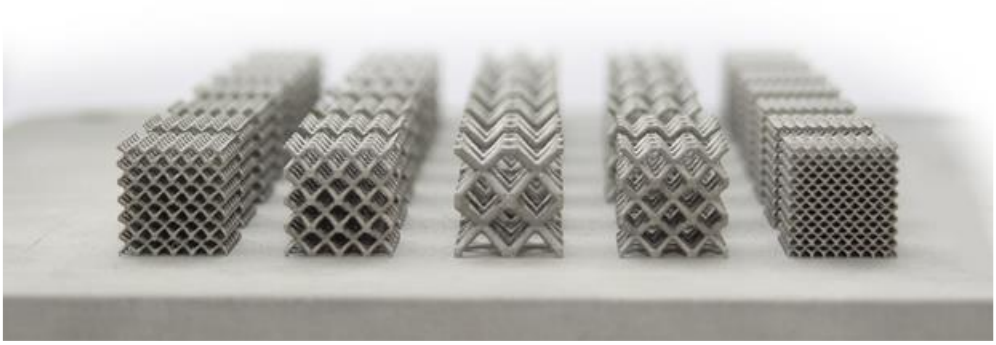

Figure 11. Lattice test structures built on Renishaw AM250 metal AM system at The University of Nottingham, as part of the Aluminium Lightweight Structures via Additive Manufacturing (ALSAM) project.

Figure 12. Spyder bracket designed and built by Altair, Materialize and Renishaw.

AM also presents opportunities for the development of functionally graded materials (FGC) because of its ability to tailor mechanical properties [10]. These materials have different mechanical characteristics throughout their volume, are known for having properties that surpass individual materials and are applied in many high technology applications, such as aerospace, civil, nuclear, semiconductor and biomedical [17]. A notorious function is to thermally shield spacecraft which walls can come to a thermal gradient as high as 1300 ºC in 10 mm thickness, a request that no monolithic material was able to achieve [18]. They can be of two forms, continuous gradation of two continuous material phases from one interface to another or change of material properties in a discontinuous, discrete form [19]. In Powder Bed Fusion (PBF, one of the main AM technologies), for example, the powder grain size and distribution can be varied to change the part's material properties, being fine particles associated with higher densities and mechanical strengths, and bigger particles with lower densities and higher breaking elongations [20].

Furthermore, there are parts that must always be complex and, traditionally, are made by multiple simple parts joined using different fastening methods, such as welds, brazes and bolts [10]. This has three main problems, lower reliability, higher inspection, tooling, and sustainment costs [21] and excessive deformations and misalignments in some cases [22]. Reducing the number of parts of an assembly has four main benefits [10], the number of tools held in inventory, the cost associated with documentation, inspection and production, the assembly line footprint and the manufacturing costs decrease. AM allows for the consolidation of parts, exploiting these four gains.

As an example, in 2018, GE (General Electric) managed to consolidate 855 parts of a Turboprop engine into 12, reducing the weight in more than 45 kg, improving fuel burn, increasing power, and simplifying maintenance [23]. On the same way, Airbus simplified a 126-parts tank

housing to one [24]. These are huge breakthroughs in engineering, the need for specific factories and machines for every part is greatly reduced and so does the final cost.

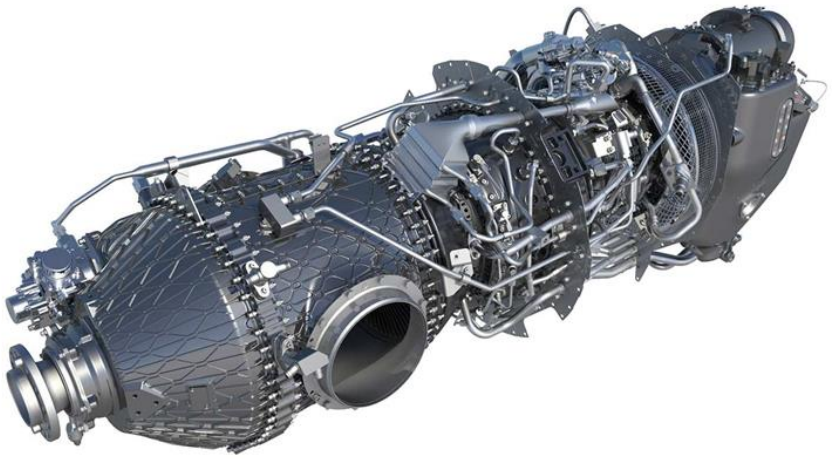

Figure 13. Turbine designed and built by General Electric that uses many 3d printed components.

However, as much as the capabilities of AM are vast, they must be economically justified. AM can reduce inventory and transportation costs by centralizing production and allowing for production on demand in many cases. For example, production of some air ducts of the F-18 Super Hornet jet were reported to have a reduction in price of more than 40%, comparing centralized production and analyzing the cost distributed on a yearly basis [25]. In this same mindset, this reduces the number of links in a supply chain while bringing production closer to customers, greatly reducing the vulnerability to unpredictable disruptions [16].

The above mentioned are mainly logistics costs. AM is also very impactful on the basic production costs. It is reported that some specific aerospace parts that are very large and thin, such as turbine blades, have very high buy-to-fly ratios (ratio between final part and raw material weights), up to 40:1 [26], meaning that a lot of expensive material is wasted. In this sense, AM allows huge cost savings, since it can have buy-to-fly ratios very close to 1:1. The Oak Ridge National Laboratory and Lockheed Martin reported a reduction from 33:1 to 1:1 in the this ratio for one specific titanium bracket of the F-35 Joint Strike Fighter jet, resulting in a 50% reduction in the total production cost of this part [27] .

Because of the AM possibility to reduce the weight by adding complexity, it is very impactful on every kind of flying machine. With SpaceX latest rocket, Falcon Heavy, the estimated payload cost is of 951 $/kg to launch objects into space [28]. Also, the reduction of 1 kg of a Boeing 737-800 aircraft accounts for an approximate 144 $ savings yearly [29]. On every industry that the parts are not produced in high quantities (where is justifiable the design of specific machines to manufacture a single part), AM can play an important economic role.

1.2.2 Metal additive manufacturing technologies

Multiple different processes are available for metal 3D printing, divided into two main categories, powder-bed, and powder-fed systems.

The first spreads the metal powder, making a flat surface with small metal grains. Then, a laser or electron beam maps this surface, melting a thin layer of this powder. A new powder layer is deposited above the first and the process is repeated, giving the part its shape. In this technology it is possible to manufacture structures with high resolution and internal passages while maintaining dimensional control [30].

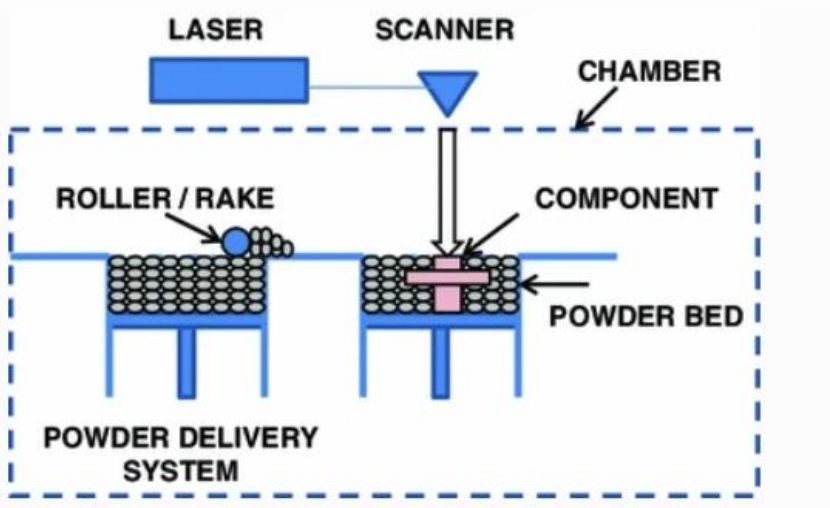

Figure 14. Representation of a powder-bed AM system.

On the other hand, powder-fed systems have the powder being constantly fed to the spot the laser is aimed at. This laser and powder head structure constantly moves to map the material layer by layer. Comparing to the powder-bed systems, it has lower resolution but higher build volumes and can also be used to repair damaged parts [30].

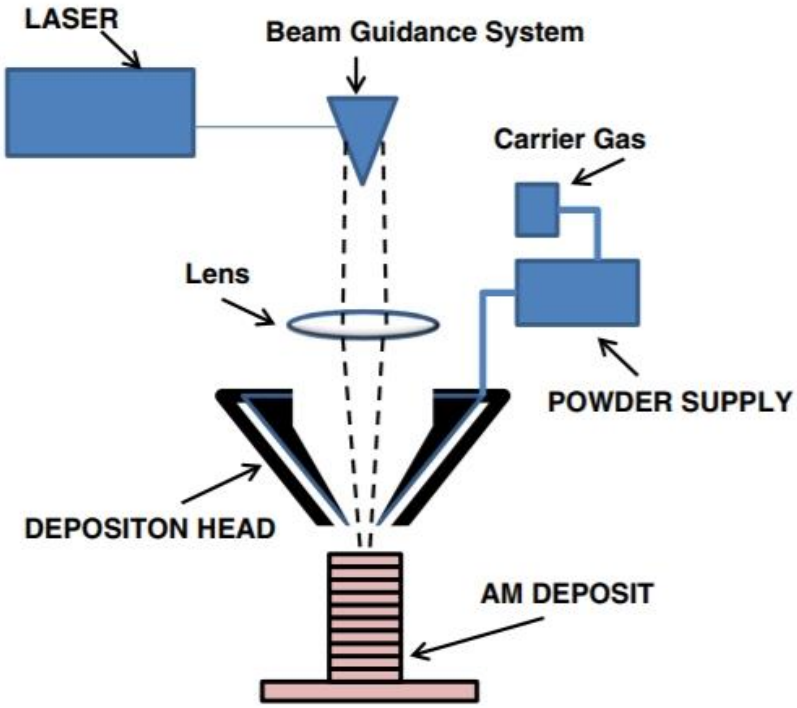

Figure 15. Representation of a powder-fed AM system.

1.2.3 Manufacturing and materials

Some characteristics of the metal AM processes makes it have very intricate metallographic structures [30]. Because of the rapid cooling, the solid solubility is reduced, sometimes generating metastable phases. The layer build-up procedure results in the heat being extracted always on the same path throughout the part, resulting in a preferred direction for grain growth which induces anisotropy. Also, thermal cycles can make the mechanical properties vary in different areas of the part and induce high residual stresses which lead to distortions. These complex behaviors are hard to be studied and there are multiple articles deeply analyzing all of them.

From these complex properties, one of the most critical is gas entrapment inside the material which generate voids inside the volume [31]. This can severely affect the fatigue resistance of the structure and, in thin structures, play a major role in inducing cracks.

In order to counter some of these referred issues, heat treatments (HT) play a major role in the AM processes. In titanium, it causes the transformation of metastable martensite into an α–β matrix, more ductile but with lower yield strength [32]. Using hot isostatic pressing (HIP) HT, the voids and porosity on a powder bed metal AM part can be significantly reduced [33] and the

strength and reliability increases [34]-[36]. In addition, solution annealing can homogenize the morphology of the built parts [37].

Metals used in current AM processes must have, in general, two characteristics: good weldability and availability in spherical powder form sized in the order of tens of microns. The first is to avoid cracking during solidification and the second is to allow good homogeneity and packing density during powder deposition [38]. There are multiple alloys that surpass this, being the most used the nickel-based superalloys (Inconel), stainless steels, titanium, and aluminum alloys. Their choice varies with the situational requirements.

In the specific case of structures that go to outer space it is essential to resist temperatures as low as -150ºC [39] . In general, aluminum, titanium, nickel, and austenitic stainless steels all retain toughness at these low temperatures, so, most AM powders should be able to be applied in these conditions, the most suitable being titanium [40], [41]. However, there is still not much literature of the analysis of these materials specifically manufactured with 3d printing.

In general, titanium AM is what gives the better strength-weight ratio and environment resistance, with main drawback being the low thermal conductivity [42]. Stainless steel is the intermediate in all mechanical properties [43]. The nickel alloys have the best resistance to high temperatures and a very high mechanical strength but also higher density [44]. Finally, aluminum is the cheapest, has good strength-weight ratio and is the most used in applications where a low weight is required, and the loading is not very high [45].

1.2.4 Topology optimization

Topology optimization in FEA is done by group of solvers that find the geometry that minimizes an objective function, under a group of constraints [46]. For example, given the material properties, boundary conditions and loads, the solver can find the best geometry (lowest mass) that is below a certain stress. Therefore, novel, and highly efficient designs can be found for any type of continuum structures [47]. AM allows for the full potential of these tools to be exploited.

There are multiple different methods to achieve optimum solutions, each with their own benefits and weaknesses. Two of the most prominent are the Solid Isotropic Structures with Penalization (SIMP) and Level-set methods.

The SIMP consists of considering the density of each FEA mesh element a design variable, thus being reduced in the regions that influence less on the given problem goals [48]-[50]. For this, a generic geometry encompassing all regions that can have material must be computer designed and have all design loads applied. Then, after the regions that cannot be modified are selected (for

example, the boundary conditions), the mesh elements have their densities iteratively changed, up to the point where the final solution is achieved. It is one of the most used methods because of the computational efficiency, robustness and allowance for most design boundary conditions to be applied [51]. The main weakness of SIMP is that it is not convex, so, does not preclude the existence of more optimized designs.

After the design iterations are complete, the result geometry must be homogenized in a CAD modeler for further analysis. Always, the load and boundary conditions must be reapplied in a separate simulation to ensure the goals were achieved. Figure 16, Figure 17 and Figure 18 are from the design procedure of a hinge of an aircraft, describing the initial geometry, the solver output, and the final homogenized solution [52]. In this case, the final weight was 25% lower than the original.

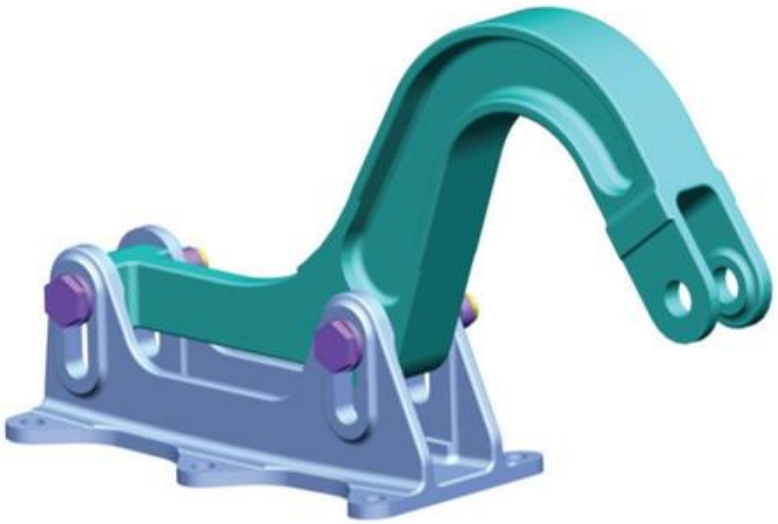

Figure 16. Initial model to be optimized. In green is the piece subject to the topology optimization analysis.

Figure 17. Raw results from the topology optimization. Needs post-processing.

Figure 18. Final results of the topology optimization, after the post-processing is finished.

The level-set method, however, deals with moving boundaries [50]. The mesh external elements are iteratively removed, so, the geometry is gradually carved from its surfaces. It is more limited than the SIMP method with respect to boundary conditions and generally cannot generate holes, which is a major drawback. Also, it is more dependent on the mesh size, being the minimum thickness achieved that of a single element [53]. Because of the different iterative procedure comparing with SIMP, the solutions found may be different for the same input conditions, so, it is essential to compare both. Figure 19 and Figure 20 show a part optimized with this type of solver.

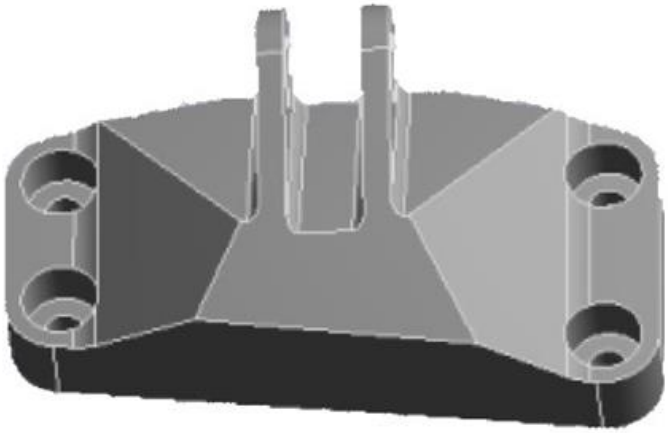

Figure 19. Piece to be optimized using the level-set method.

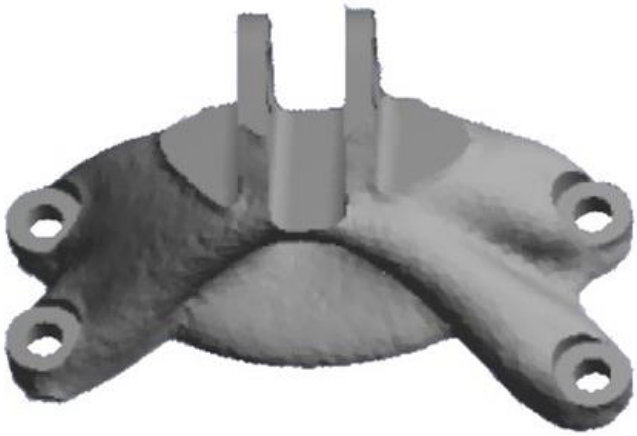

Figure 20. Raw results of the level-set based optimization.

Also, there are lattice optimization solvers which are a variation of the regular density-based solver (SIMP). They create an irregular lattice structure, with variable density throughout its volume in a similar iterative procedure as that of SIMP. The main difference is that there is a limitation on the minimum density obtained because of the minimum element arm diameter (see Figure 21 for this dimension). One big drawback is the complex procedure required to generate the geometry after the analysis, because of its high complexity and errors when the minimum density

is very small. On Figure 21 there are four different possible element types, with the names given by the author.

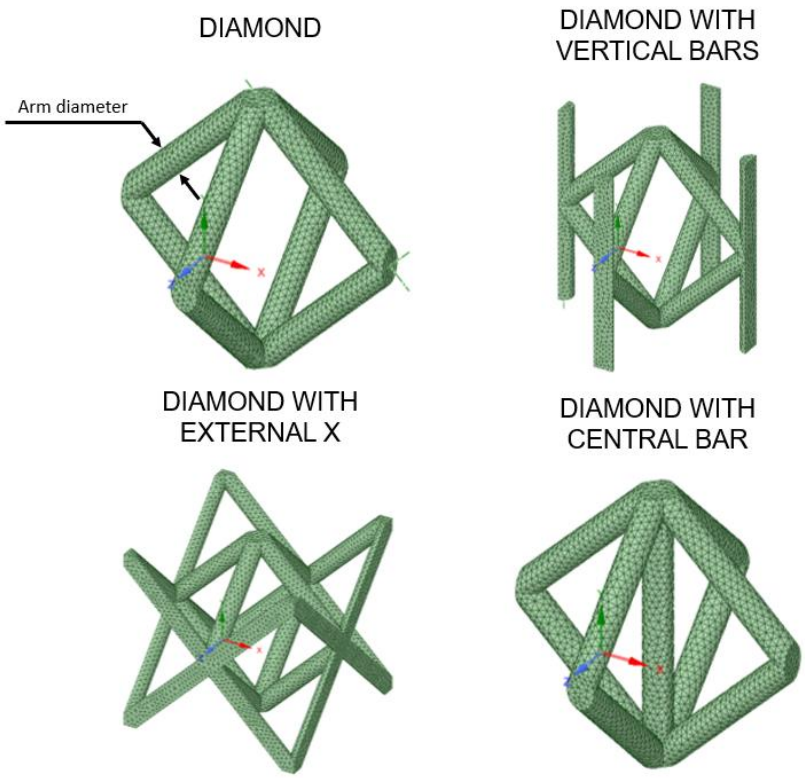

Figure 21. Different types of lattice elements. There are many more possible designs, these were given names by the author and will be further used in this project work.

2 Methodology

2.1 Functional requirements and loading conditions

All design goals but the acceleration loads were the same as the model designed and manufactured previously, described in section 1.1. For this changed parameter, a new approach was done to better consider the defects and unpredictability of the component manufactured by 3D printing.

The new acceleration was defined by the base required load resistance of 700 m/s² for the landing conditions and the European Cooperation for Space Standardization (ECSS) standard ECSS-E-ST-32-10C Rev.2 Corrigendum 1, which informs about design factors for the engineering of space structures [54]. From there, five different coefficients were defined and applied at the design load.

Firstly, the model factor (Km), which accounts for the uncertainties of the mathematical model, was considered 1.2, as suggested in the document for "satellites on the beginning of new development". In our case, it accounts for the bolt fixation load both of the mirror assembly to the pendulum arm and of the whole mirror and pendulum arms assembly to the shaft. This load was not considered in the FEA as a simplification.

The second, project factor (Kp), is due to the design maturity. This was set to 1 as this project was done and tested previously, so, confidence in the model is high.

After this, was considered the qualification test factor (KQ), a parameter applied to satellites. It is 1.25 as specified in the Table 4-2 of the standard.

The fourth factor, local design factor (Kld), accounts for the presence of complex local structures which cannot be properly modelled and accounted for. These, in our case, are small vertexes (which were avoided as much as possible in the design by the use of fillets), lattice structure possible manufacturing discontinuities and the presence of voids due to the SLM (Selective Laser Melting) process [55] (manufacturing process of the AM machine used on this project). In the document is said that a coefficient of 1.2 is used for composite and sandwich structures discontinuities, therefore, we used this same value in our design.

Lastly, the yield design factor of safety (FOSY) is considered. According to the Table 4-4 of the document, a FOSY of 1.1 is used for satellites that were also test verified, which is the case of the previous MIMA design. Thus, 1.1 was the value considered.

Finally, the design load of 1386 m/s² is found, which will be used at all acceleration design analysis.

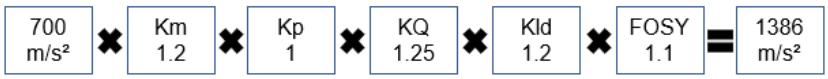

Figure 22. Representation of the calculation procedure to reach the final acceleration input.

2.2 Design constraints

In general, AM parts can be built with any geometry regarding that there are support structures to anchor overhangs (their absence can generate distorted and curled structures [56]). However, by having supports, material is wasted and there are higher requirements for manufacturing post-processing since the supported surfaces are usually rougher [57]. The general guideline for maximum AM overhang angle is 45º [33], therefore, on this design study, high efforts will pe put towards this. Also, previous attempts to manufacture using the available machine (AM400 Renishaw), indicated that it could properly 3d print structures with thickness of 0.5 mm or more, values below this presented excessive distortions and voids which severely harm the final quality and reliability. Thus, this will be the minimum thickness used.

2.3 Materials

The main material requirements were commercial availability and not being fragile at temperatures below 120 ºC. Table 2 contains the properties of the metal powders offered by Renishaw that surpass these conditions [42]-[45]. This is the same brand as the AM machine to be used. For the yield strength (YS), the data inserted is for (Mean – 2*Standard deviation) and of lowest axis (the data informed on the datasheets contains the YS as a function of the axis because of AM parts anisotropy behavior).

Material	Density [g/cm³]	Yield Strength [MPa]	Strength/density ratio	Modulus of elasticity [GPa]	Thermal conductivity [W/mK]
316L Stainless steel As built	7.99	466	58.3	170	16
AlSi10Mg Stress relieved	2.68	203	75.7	66	160
Ti6Al4V HIP treated	4.42	881	199	117	7
Inconel 718 HIP treated	8.19	1036	126.5	195	9

Table 2. Properties of the materials considered for this project's design

The best among them is the material that provides the part with the smallest weight. As will be further seen, there is a region that cannot be modified and has a considerable influence on the final weight. Because of this, even if titanium has a better strength-weight ratio, aluminum is the best choice because of the smaller density. Also, aluminum has one of the highest thermal conductivity coefficients of all metals, so, has increased safety in case there are high thermal gradients on the part.

3 Single pendulum arm design

3.1 Introduction

This section describes the redesign of a single pendulum arm using five different methods: Honeycomb structures, ANSYS material designer, topology optimization, lattice optimization and optimization of just an external plate. The design constraints, the best design choice criteria, FEA model and the specific methods are described as follows.

3.2 Design constraints and optimization region

In order to keep the same alignment procedure as the previous pendulum arm model, the three bolts and the spherical joint regions from the pendulum arm were chosen to be kept totally unchanged. Back then, this was a major issue and since this solution had worked perfectly, it was preferred to be kept as it is.

Then, the first step was to isolate both of these parts from the model and generate a solid geometry, which would be the “optimizable region”, the only region in the model that can have changes. For this, the previous model was cut, both on the region between the three bolts and the spherical joint and after the three bolts. The 0.5 mm minimum wall thickness was kept around the bolt holes and the minimum spherical joint wall size was not changed. The mass of this unchanged part is 7.43 g. The comparison between the previous model and the one after the changes is in Figure 23.

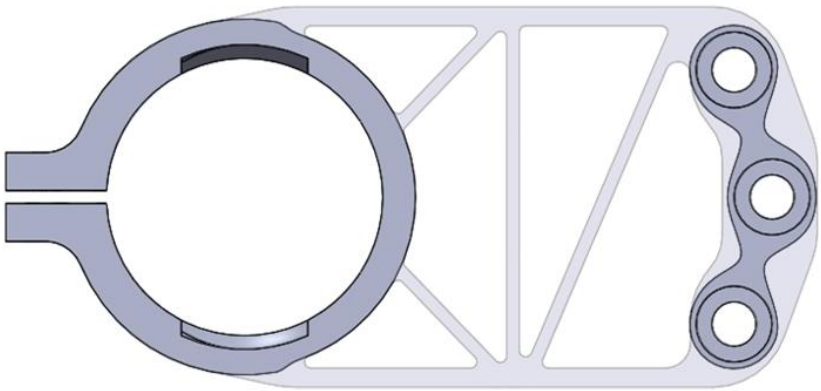

Figure 23. Comparison between the previous model and region selected to be kept unchanged on all analysis done. The transparent region is what was deleted from the previous model.

After this, a region between these two areas was drawn, the so called “optimizable region”. It is shown in Figure 24.

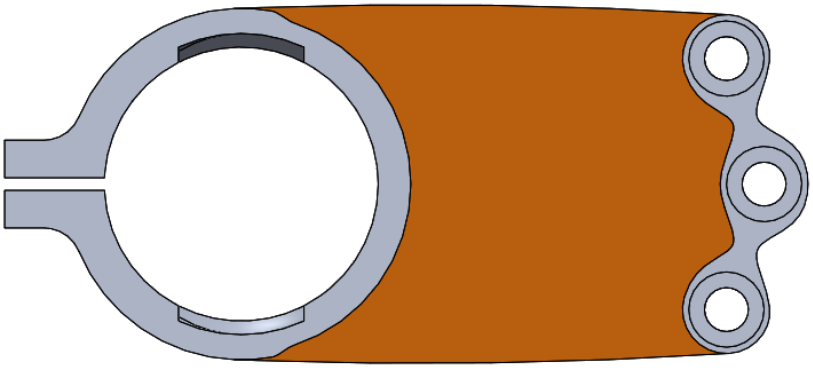

Figure 24. In orange is the optimizable region, the only part of the model that can be modified for the analysis done.

3.3 Choice of the best solution

Since many different approaches were used to reach a result, a mathematical model must be defined to choose the best. The basic goal is to reduce mass while respecting the minimum first natural frequency and maximum stress (from the stress relieved AlSi10Mg, 203 MPa) constraints. Because of this multitude of variables, a multi-objective optimization approach was used, with three different coefficients which sum characterizes each design’s grade.

The first coefficient defines the mass influence. Its behavior is such that lower the mass, higher is the coefficient, up to a maximum of one. Then, parting from the “non-optimized mass” of 7.43 g, it has a linear behavior, being 1 for 7.43 g and 0 for 14.60 g, the mass of the previous design. The graph XX defines how it behaves. Its function is:

$$Km = (Mass - 7.43)/(14.60 - 7.43)$$

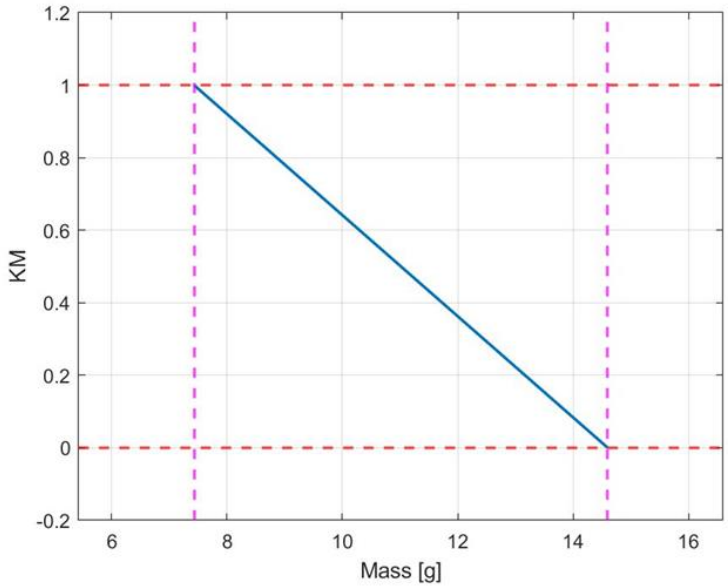

Figure 25. Evolution of the mass coefficient according to the pendulum arm`s total mass.

Going on, the second coefficient varies with the value of the first natural frequency (FNF), which must be at least of 140 Hz. It is not beneficial to have a too high FNF because it means the part has more mass than it is needed, then, the coefficient was built in such way that it tends to one for high enough values of the FNF, being 0.2 when it is 140 Hz. Below is a table with its desired behavior.

Frequency	Coefficient
140 Hz	0.20
200 Hz	0.50
350 Hz	0.95
600 Hz	0.99
1000 Hz	1.00

Table 3. Frequency coefficient variation according with the pendulum arm's first natural frequency value.

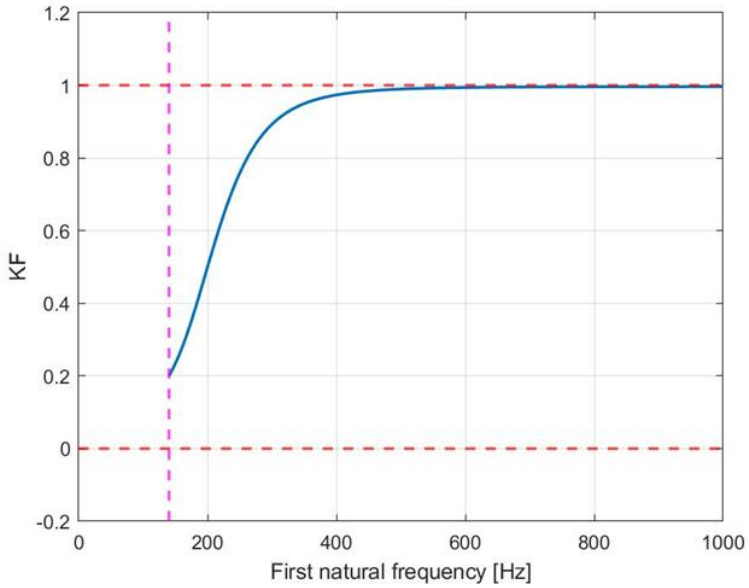

Figure 26. Graph of the frequency coefficient as a function of the first natural frequency of the pendulum arm. For high enough frequencies, it tends to 1.

Finally, the third coefficient accounts for the part design, it is a way of accounting for the maturity and predictability of each different model. For the previous model, this value is one because it was already designed and tested. For all analyzed models that are not made of lattices, it is of 0.9, because there is high trust that its behavior when manufactured will be very similar of that of the designed.

For the designs with lattice structures, this coefficient varies in a cubic manner with its lattice element length, from 0.55 to 0.85. The logic behind it is that with larger lattice sizes there are less lattice elements in the geometry so, if there is a manufacture defect in its structure, this defect has a higher impact on the load paths. It varies in a cubic manner because the number of lattice elements is inversely proportional to the cubic potency of its element length. Table 4 has this coefficient's value for each lattice element length that was used in this study.

Lattice length	Coefficient
2.00 mm	0.85
2.50 mm	0.85
3.33 mm	0.85
5.00 mm	0.81
10.00 mm	0.55

Table 4. Design coefficient variation according to the lattice element length.

By summing these three coefficients, the design grade is defined and then the different geometries achieved can be compared.

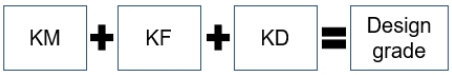

Figure 27. Representation of the calculation procedure to reach the final design grade.

3.4 FEA Model

3.4.1 Constraints and their equivalent on the FEA model (boundary conditions)

All FEA of this study was done on ANSYS 2019 R2 due to the author previous experience with this program. More than ten trials, with multiple different boundary conditions were done to reach this final FEA model version. The result was considered positive because it is simple and able to properly approximate the actual behavior of the pendulum arm.

The three bolts and spherical joint regions are located where the boundary conditions must be applied. For the bolts, both the bolt head and the part where the pendulum arm touches the shaft assembly are a Y direction displacement constraint, and the bolt hole is a radial direction displacement constraint. For the spherical joint, its region was considered rigid to mimic how it behaves when the mirror is fastened in place. Also, a Point Mass representing the mirror assembly mass/inertia, located on the mirror assembly geometric center, was connected to the spherical joint inner faces. These boundary conditions are shown on Figure 28, Figure 29, Figure 30, Figure 31 and Figure 32.

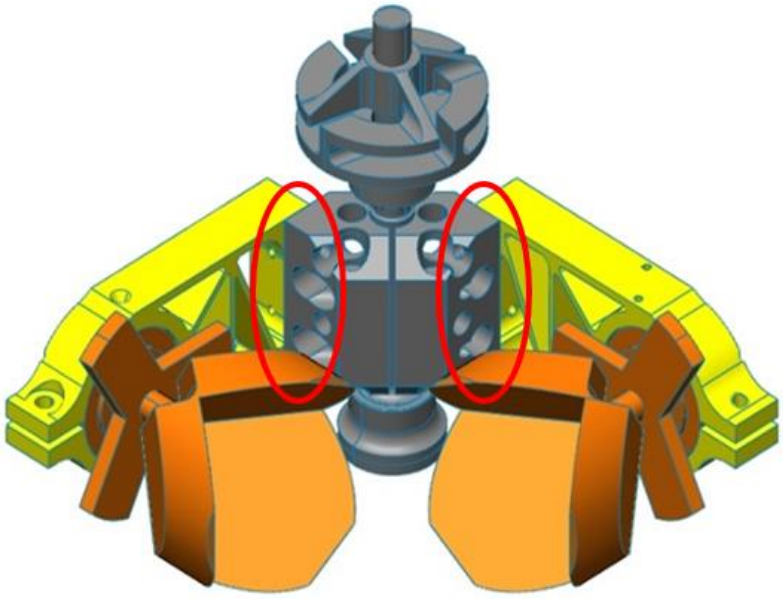

Figure 28. Pendulum arms and shaft assembly. In red, the region where the pendulum arms touch the shaft assembly.

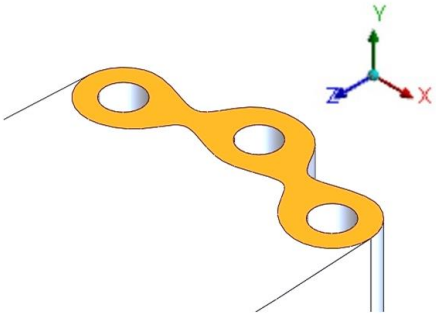

Figure 29. In orange, region where pendulum arm touches the shaft assembly. This region has the Y displacement constrained and free X and Z displacement.

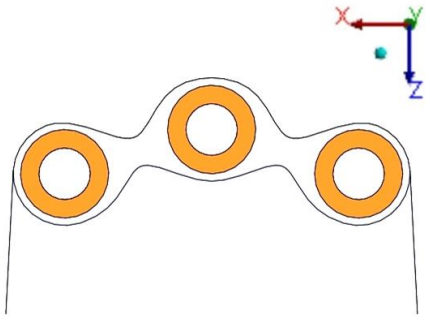

Figure 30. In orange, region where the bolt head is applying force. This region has the Y displacement constrained and free X and Z displacement.

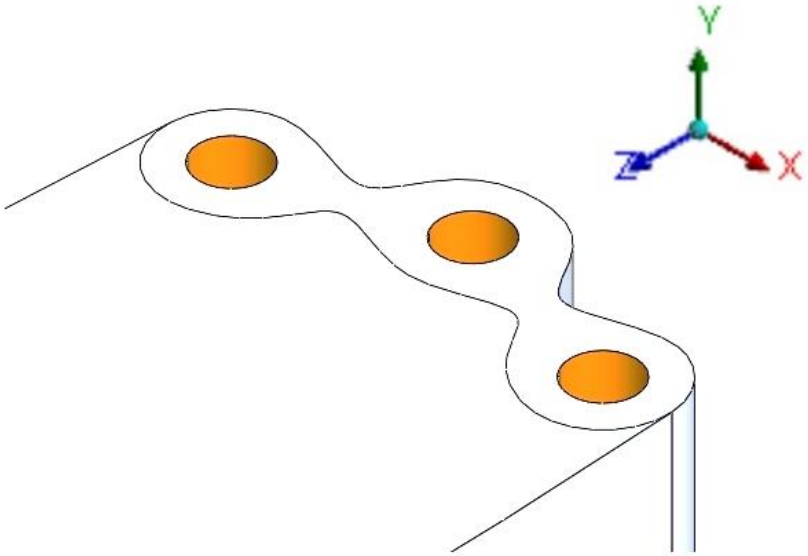

Figure 31. In orange, region where the bolt body is located. This region has a cylindrical support with radial displacement constrained and free axial and tangential displacement.

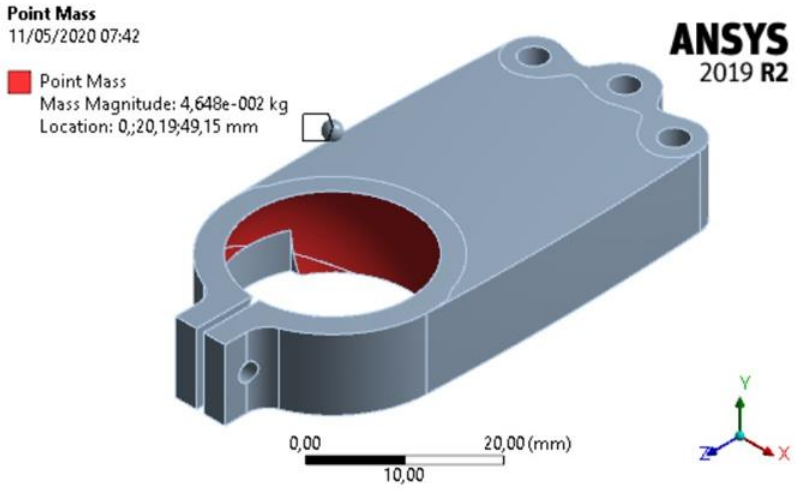

Figure 32. Point mass in the model. The red surfaces are where the point mass is connected (they are rigid) and the sphere above them is the point mass location.

3.4.2 Mesh

The mesh, in nearly all models analyzed, was done with ANSYS adaptive sizing and the highest possible resolution. This generates tetragonal elements that are refined on the edges based on curvature and proximity [58]. The goal was to keep the average element quality (measure of how close each element is to its regular form [58]) above 0.7 and have a large enough quantity of elements to do the optimizations (at least 8 elements through its thickness). A view of it is on Figure 33.

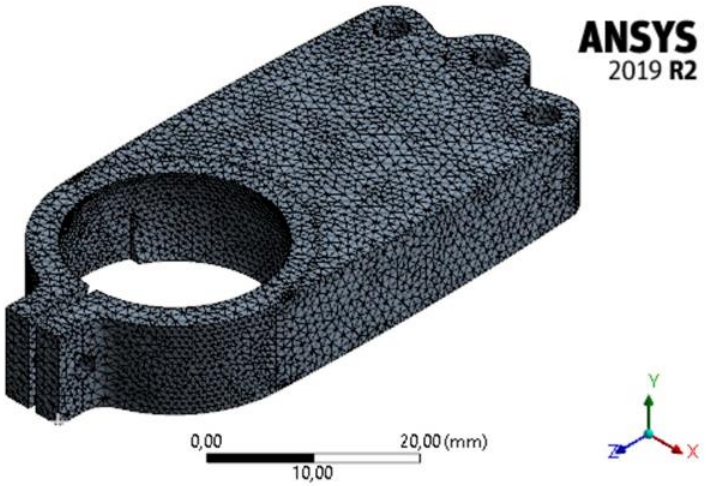

Figure 33. Surface mesh of the single pendulum model, with tetragonal elements.

3.4.3 Description of the static model (acceleration)

As for the previous MIMA design, the acceleration load can be active in any direction. At this design, the total load of 1386 m/s² was applied on the three axis of Figure 38. The higher stresses were found when the acceleration was on the Y and on the X directions. Then a third direction was tested, the +X +Y, which found stresses higher than the X or Y cases, so, this was the chosen direction for comparison on all initial analysis. For the chosen designs at the end of this chapter, all possible directions will be retested, in order to fully validate it. The stress considered is always the Equivalent Von-Mises.

3.4.4 Description of the dynamic model (vibration modes)

The dynamic analysis is a regular modal simulation, where mode shapes and natural frequencies are found based on the boundary conditions and mass/inertia inputs. When showing the results of this section, mode shapes were assigned names and on Figure 34, Figure 35, Figure 36 and Figure 37, these names are attributed to the shapes deformations.

Figure 34. Mode shape named by the author as lateral bending.

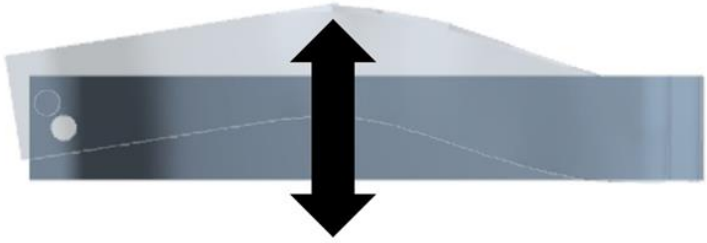

Figure 35. Mode shape named by the author as middle bending.

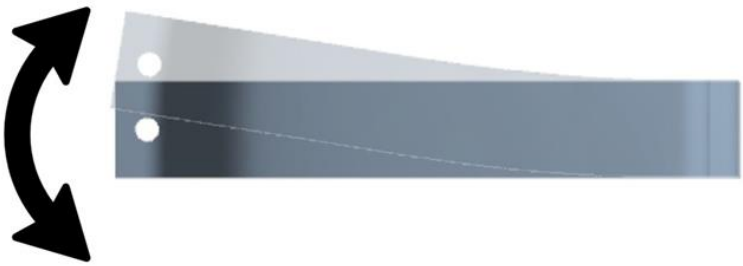

Figure 36. Mode shape named by the author as regular bending.

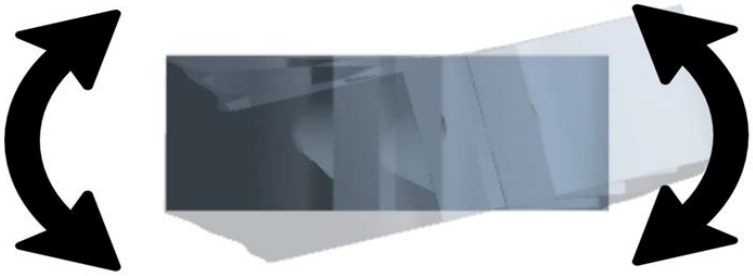

Figure 37. Mode shape named by the author as torsion.

3.5 Solutions analyzed

On this section, the models and results from all different methods are described. Initially no focus was given to the maximum stress because a huge quantity of designs was analyzed, and it would be too time consuming to get proper stress convergences for each. Then, the adopted procedure was:

(1) Initial analysis just considering each design's grade. Choice of the best designs.
(2) Stress analysis using the direction +X +Y explained in section 3.4.3 and do iterative design changes, adding material where stress is above the threshold. From these modified designs, new grades are defined.
(3) Comparison between the model with highest grade of each method and choice of the two best to be further analyzed for stress convergence.
(4) Stress converge analysis of the two overall best geometries and final discussion.

3.5.1 Previous model analysis

3.5.1.1 Method explanation

As a first step, the previously designed model was reanalyzed, to have its results for comparison. Figure 38 shows its geometry.

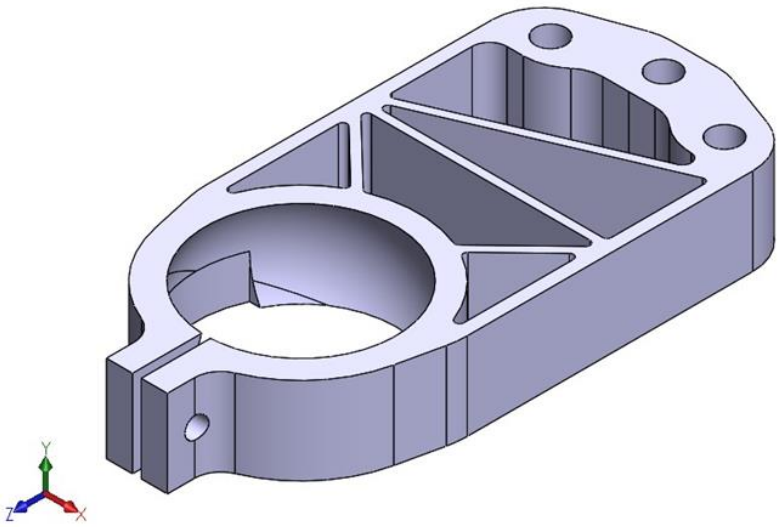

Figure 38. Solidworks image of the previous pendulum arm model.

3.5.1.2 Results and comments

Since the first natural frequency is way higher than the minimum and the stress is far from the maximum, we know this can be further optimized. On the further models it will be seen that the grade can be greatly improved.

Name	Mass	1st nat.freq.	1st shape	2nd nat.freq.	2nd shape	3rd nat.freq.	3rd shape	GRADE	Stress
Previous design	14.60 g	489 Hz	Regular bending	899 Hz	Torsion	2303 Hz	Middle bending	**1.99**	37 MPa

Table 5. Analysis table of the previous pendulum arm model.

3.5.2 Honeycomb models

3.5.2.1 Method explanation

On this method, honeycomb structures were generated inside the optimizable region, always with the 0.5 mm minimum thickness and with varying hexagon sizes. Care was taken to keep it always centralized, spaces where there would be tight angles were softened with fillets and very small gaps were filled. The hexagon size varied from 4 mm to 12 mm, and in some cases minor changes were done to the hexagon position to study if there were changes on the frequency results. Figure 39 and Figure 40 show two examples, for 6mm and 11mm sizes.

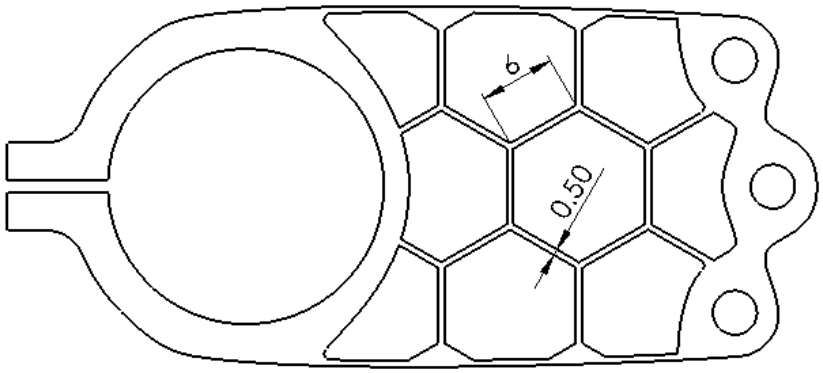

Figure 39. 6 mm length honeycomb.

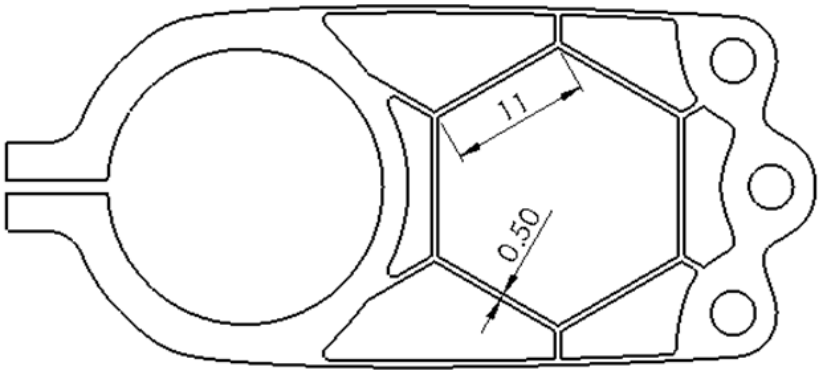

Figure 40. 11 mm length honeycomb.

3.5.2.2 Results and comments

Based on Table 6, the 6 mm and 11 mm versions were chosen to be further developed. Initially, the stresses were high, 206 MPa for the 6 mm case and 252 MPa for the 11 mm one. Then, material was added on the regions with highest stress, as described on Figure 41, to lower these values. Thus, the masses increased, and new grades must be calculated.

Name	Mass	1st nat.freq.	1st shape	2nd nat.freq.	2nd shape	3rd nat.freq.	3rd shape	GRADE
Honeycomb 4mm	11.37 g	394 Hz	Regular bending	499 Hz	Lateral Bending	1263 Hz	Torsion	**2.32**
Honeycomb 5mm	11.09 g	368 Hz	Regular bending	471 Hz	Lateral Bending	1184 Hz	Torsion	**2.35**
Honeycomb 6mm	10.52 g	344 Hz	Lateral Bending	354 Hz	Regular bending	933 Hz	Torsion	**2.41**
Honeycomb 6mm_v2	11.05 g	358 Hz	Regular bending	362 Hz	Lateral Bending	975 Hz	Torsion	**2.35**
Honeycomb 7mm	10.18 g	287 Hz	Lateral Bending	343 Hz	Regular bending	867 Hz	Torsion	**2.38**
Honeycomb 7mm_v2	10.26 g	297 Hz	Lateral Bending	357 Hz	Regular bending	871 Hz	Torsion	**2.39**
Honeycomb 8mm	10.20 g	280 Hz	Lateral Bending	337 Hz	Regular bending	867 Hz	Torsion	**2.37**
Honeycomb 8mm_v2	10.24 g	286 Hz	Lateral Bending	347 Hz	Regular bending	868 Hz	Torsion	**2.37**
Honeycomb 9mm	10.20 g	268 Hz	Lateral Bending	329 Hz	Regular bending	870 Hz	Torsion	**2.33**
Honeycomb 9mm_v2	10.16 g	291 Hz	Lateral Bending	343 Hz	Regular bending	879 Hz	Torsion	**2.40**
Honeycomb 10mm	10.01 g	253 Hz	Lateral Bending	337 Hz	Regular bending	902 Hz	Torsion	**2.31**
Honeycomb 10mm_v2	10.23 g	293 Hz	Lateral Bending	336 Hz	Regular bending	889 Hz	Torsion	**2.39**
Honeycomb 11mm	10.10 g	333 Hz	Regular bending	351 Hz	Lateral Bending	959 Hz	Torsion	**2.46**
Honeycomb 12mm	10.18 g	339 Hz	Regular bending	354 Hz	Lateral Bending	988 Hz	Torsion	**2.46**

Table 6. Analysis table of the models developed with the honeycomb method.

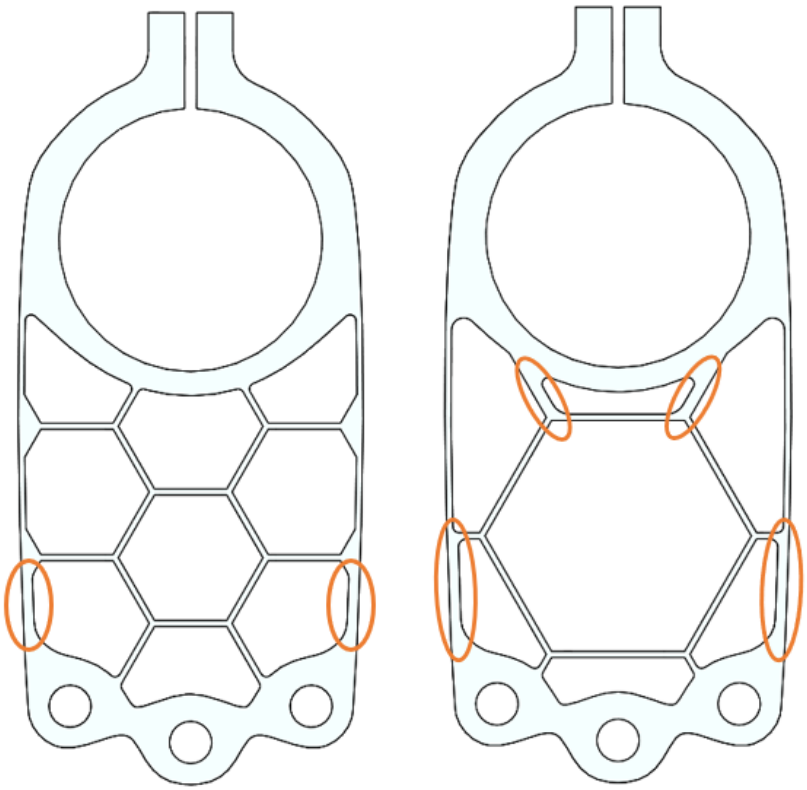

Figure 41. In orange are the changes done to ensure the stress is inside the threshold. On the left is for the 6 mm length honeycomb and on the right for the 11 mm length honeycomb.

Table 7 contains the new results, also with new grades for each. The 11 mm case was the best of both and will be used in the further comparisons.

Name	Mass	1st nat.freq.	1st shape	2nd nat.freq.	2nd shape	3rd nat.freq.	3rd shape	GRADE	Stress
Honeycomb 6mm_final	10.68 g	372 Hz	Lateral Bending	385 Hz	Regular bending	1035 Hz	Torsion	**2.41**	152 MPa
Honeycomb 11mm_final	10.51 g	377 Hz	Regular bending	505 Hz	Lateral Bending	1285 Hz	Torsion	**2.44**	183 MPa

Table 7. Analysis table of the best models developed with the honeycomb method.

3.5.3 Material designer models

3.5.3.1 Method explanation

On this section, the analysis is done mainly with ANSYS Material Designer tool [59]. Its use is to homogenize material properties of periodic complex structures, such as lattices and composites by approximating their properties to a solid material. In this study's case, it calculates which properties (anisotropic elastic/shear modulus, Poisson's ratio, and density) a solid material must have to behave like a lattice structure with certain given characteristics (shape, arm diameter, and length).

In order to respect the 45º overhang limitation, the lattice possibilities were very limited. Four different shapes, all based on the regular "diamond" lattice were analyzed, always with 0.5 mm arm diameter and with element lengths of 2 mm, 2.5 mm, 3.33 mm, 5mm and 10 mm, which are integer multiples of the pendulum arm height of 10mm.

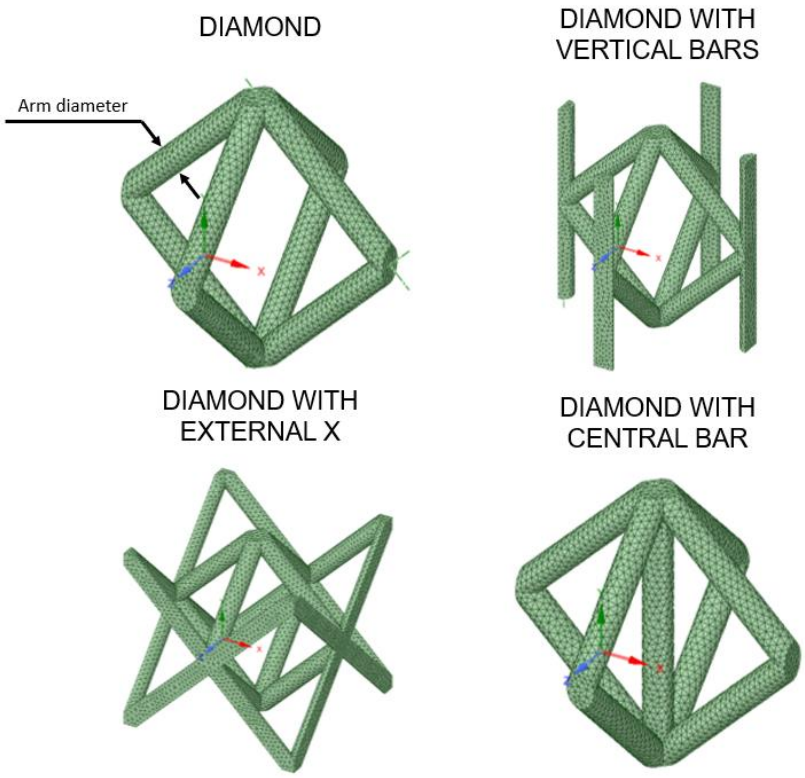

Figure 42. Different types of lattice elements used in this project work. These were the only selected because they attend the 45° overhang constraint. Names were given by the author.

When the new material properties are defined, they were used in a modal analysis, having the same boundary conditions as those explained in section 3.4.1. The region in orange of Figure 43 was where the newly generated materials were applied to.

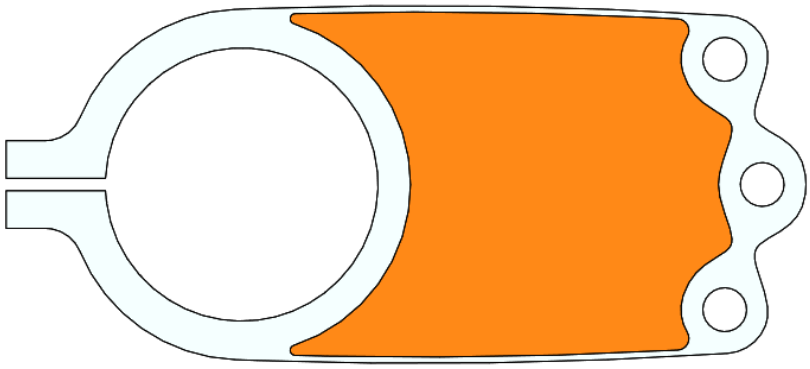

Figure 43. In orange is the region where the material designer equivalent material is applied.

3.5.3.2 Results and comments

From Table 8, Table 9, Table 10 and Table 11, four were chosen to be further analyzed: Diamond 3.33 mm, Diamond 5 mm, Diamond with central bar 5mm and Diamond with external X 5 mm. As can be seen, these are not the designs with the absolute highest grades. According to this, Diamond 5 mm is the best, but when it was analyzed on stress (as will be further described in this section), it had very high stress values, more than 350 MPa. Then, other 5mm lattices (both denser than the Diamond 5 mm) were also picked to study if this stress problem would be solved.

Name	Mass	1st nat.freq.	1st shape	2nd nat.freq.	2nd shape	3rd nat.freq.	3rd shape	GRADE
Diamond 2mm	12.29 g	445 Hz	Regular bending	869 Hz	Lateral Bending	2263 Hz	Torsion	**2.16**
Diamond 2.5mm	10.29 g	386 Hz	Regular bending	748 Hz	Lateral Bending	1927 Hz	Torsion	**2.42**
Diamond 3.33mm	9.74 g	339 Hz	Regular bending	630 Hz	Lateral Bending	1623 Hz	Torsion	**2.47**
Diamond 5mm	8.82 g	303 Hz	Regular bending	519 Hz	Lateral Bending	1357 Hz	Torsion	**2.51**
Diamond 10mm	8.25 g	280 Hz	Regular bending	413 Hz	Lateral Bending	1108 Hz	Torsion	**2.29**

Table 8. Analysis table of the models developed with the material designer method with diamond elements.

Name	Mass	1st nat.freq.	1st shape	2nd nat.freq.	2nd shape	3rd nat.freq.	3rd shape	GRADE
Diamond w/ vert. bar 2mm	13.49 g	484 Hz	Regular bending	913 Hz	Lateral Bending	2445 Hz	Torsion	**1.99**
Diamond w/ vert. bar 2.5mm	11.74 g	402 Hz	Regular bending	767 Hz	Lateral Bending	2004 Hz	Torsion	**2.22**
Diamond w/ vert. bar 3.33mm	10.27 g	344 Hz	Regular bending	639 Hz	Lateral Bending	1653 Hz	Torsion	**2.40**
Diamond w/ vert. bar 5mm	9.08 g	304 Hz	Regular bending	522 Hz	Lateral Bending	1364 Hz	Torsion	**2.48**
Diamond w/ vert. bar 10mm	8.31 g	280 Hz	Regular bending	410 Hz	Lateral Bending	1094 Hz	Torsion	**2.28**

Table 9. Analysis table of the models developed with the material designer method with diamond with vertical bar elements.

Name	Mass	1st nat.freq.	1st shape	2nd nat.freq.	2nd shape	3rd nat.freq.	3rd shape	GRADE
Diamond w/ external X 2mm	15.81 g	573 Hz	Regular bending	1145 Hz	Lateral Bending	2941 Hz	Torsion	**1.67**
Diamond w/ external X 2.5mm	13.39 g	473 Hz	Regular bending	959 Hz	Lateral Bending	2431 Hz	Torsion	**2.01**
Diamond w/ external X 3.33mm	11.29 g	393 Hz	Regular bending	783 Hz	Lateral Bending	1978 Hz	Torsion	**2.28**
Diamond w/ external X 5mm	9.59 g	330 Hz	Regular bending	614 Hz	Lateral Bending	1568 Hz	Torsion	**2.44**
Diamond w/ external X 10mm	8.45 g	288 Hz	Regular bending	461 Hz	Lateral Bending	1236 Hz	Torsion	**2.28**

Table 10. Analysis table of the models developed with the material designer method with diamond with external X elements.

Name	Mass	1st nat.freq.	1st shape	2nd nat.freq.	2nd shape	3rd nat.freq.	3rd shape	GRADE
Diamond w/ centr. bar 2mm	12.80 g	465 Hz	Regular bending	885 Hz	Lateral Bending	2353 Hz	Torsion	**2.09**
Diamond w/ centr. bar 2.5mm	11.29 g	394 Hz	Regular bending	756 Hz	Lateral Bending	1998 Hz	Torsion	**2.28**
Diamond w/ centr. bar 3.33mm	10.00 g	342 Hz	Regular bending	636 Hz	Lateral Bending	1643 Hz	Torsion	**2.44**
Diamond w/ centr. bar 5mm	8.96 g	305 Hz	Regular bending	524 Hz	Lateral Bending	1371 Hz	Torsion	**2.50**
Diamond w/ centr. bar 10mm	8.27 g	280 Hz	Regular bending	411 Hz	Lateral Bending	1094 Hz	Torsion	**2.29**

Table 11. Analysis table of the models developed with the material designer method with diamond with central bar elements.

As the next step, true models were generated with the four chosen lattice configurations. This is done by substituting the region in orange of Figure 43 by the lattice solid model. An example is on Figure 44, of the Diamond 3.33 mm. On all of them, stress surpassed the 203 MPa threshold, being higher on the lateral walls and sometimes also inside the lattice structures. Then, changes, as described in Figure 45, were done in each of the models to respect the maximum stress. This was an iterative procedure, with minor changes at each new model so that mass is increased the minimum possible.

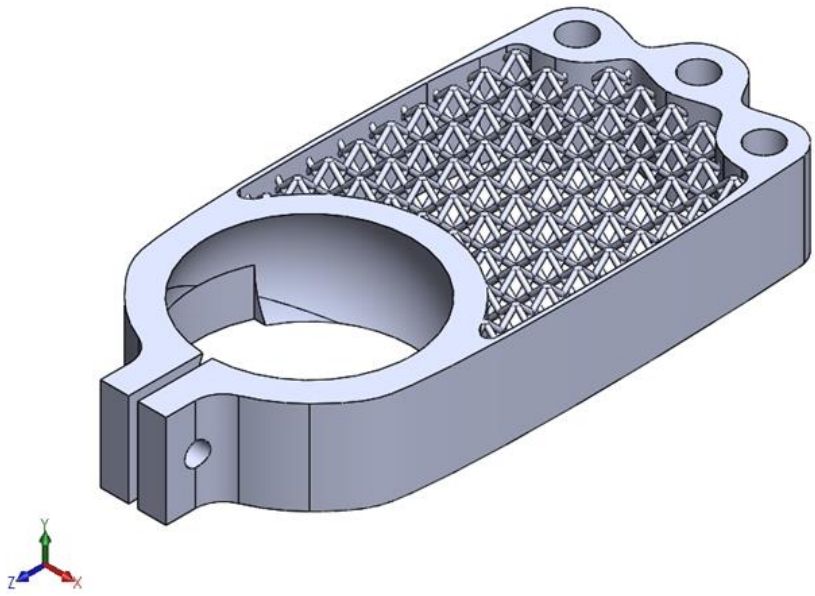

Figure 44. True model of a pendulum arm filled with 3.33 mm diamond lattice elements.

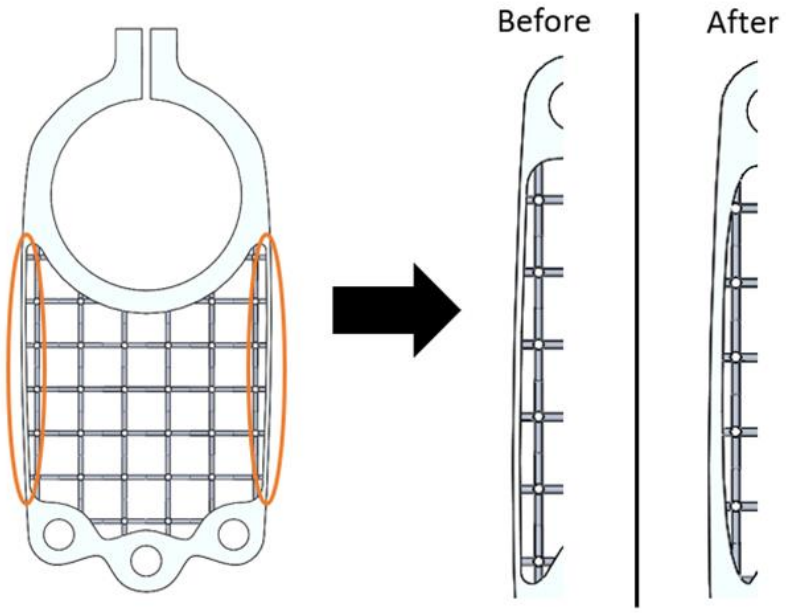

Figure 45. Increase in lateral wall thickness to keep the maximum stress below the 203 MPa threshold.

From Table 12 can be concluded that the grades for the 5 mm lattices greatly reduced because of the lateral wall thickness increase to reach the maximum stress threshold. Also, the approximations done with the material designer yielded higher natural frequencies than those of the true lattices. This probably was caused by the connections between the solid material (orange in Figure 43) to the walls surrounding it, that has a bigger area than that of the true lattice.

In this section the best design was the Diamond 3.33 mm.

Name	Mass	1st nat.freq.	1st shape	2nd nat.freq.	2nd shape	3rd nat.freq.	3rd shape	GRADE	Stress
Diamond 3.33mm_lat	9.83 g	316 Hz	Lateral Bending	328 Hz	Regular bending	890 Hz	Torsion	**2.43**	159 MPa
Diamond 5mm_lat	9.74 g	251 Hz	Lateral Bending	374 Hz	Regular bending	1022 Hz	Torsion	**2.25**	195 MPa
Diamond w/ external X 5mm_lat	10.02 g	310 Hz	Lateral Bending	353 Hz	Regular bending	954 Hz	Torsion	**2.36**	181 MPa
Diamond w/ centr. bar 5mm_lat	10.10 g	294 Hz	Lateral Bending	407 Hz	Regular bending	1084 Hz	Torsion	**2.32**	200 MPa

Table 12. Analysis table of the best models developed with the ANSYS material designer method.

3.5.4 Topology optimization models

3.5.4.1 Method explanation

For the topology optimization (TO), the whole optimizable region is selected as the scope of the simulation. In this type of analysis ANSYS Mechanical has two solvers, Density based, and Level-set based, both explained in section 1.2.4. Also, two different ways of doing the modal TO were identified, one minimized the mass while keeping a constraint on the first natural frequency and the other maximized the first natural frequency with a constraint on the reduction of mass. Then, there is a total of four different combinations. Also, constraints were imposed to have X and Y axis symmetry, as shown in Figure 47 and Figure 48.

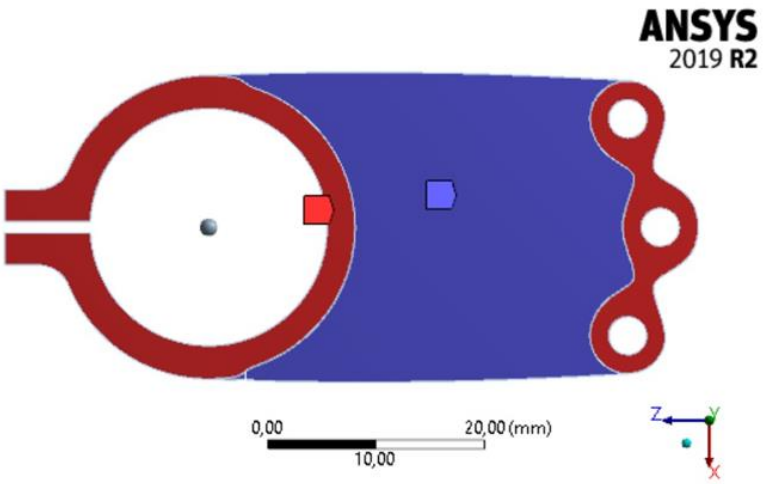

Figure 46. Design region (blue) and exclusion region (red) used in the TO.

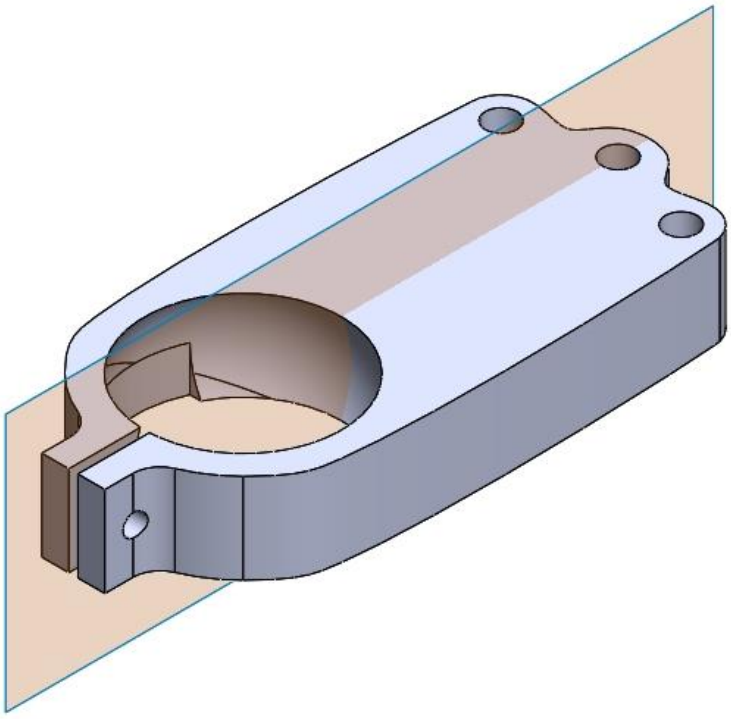

Figure 47. In orange is one of the symmetry planes inputted in the TO analysis.

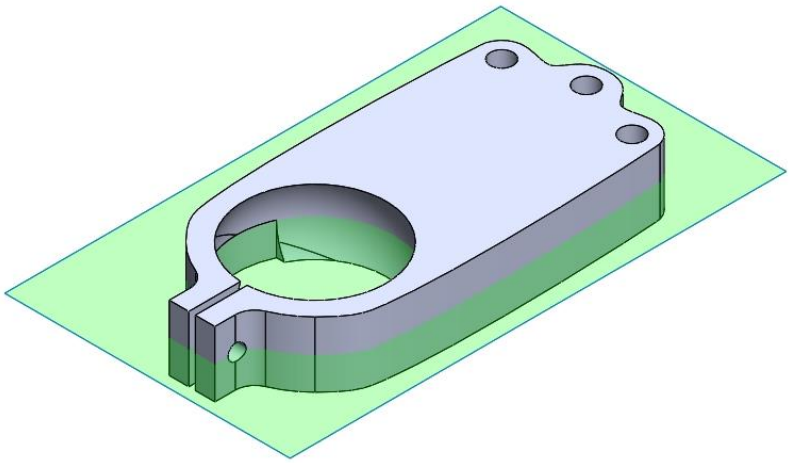

Figure 48. In green is one of the symmetry planes inputted in the TO analysis.

3.5.4.2 Results and comments

Many trials with different parameters on both ways of doing the TO were done. The results displayed are for the first natural frequency constraint of 300-320 Hz in the first “minimum mass” case and 5-15 % of the original mass on the “maximum first natural frequency” case.

None of the two Level-set based analysis gave proper results. This was expected due to the behavior of this solver, it works changing surfaces, therefore can’t produce shapes with material only on the outer walls which is the region with most influence on the stiffness (better explained in section 3.5.6.1). An example is in Figure 49, which is known not to be an optimal case because having material in the central region is what generates the minimum stiffness on Y and X direction loads and Z torsions. Therefore, the results from the Level-set solver were disregarded.

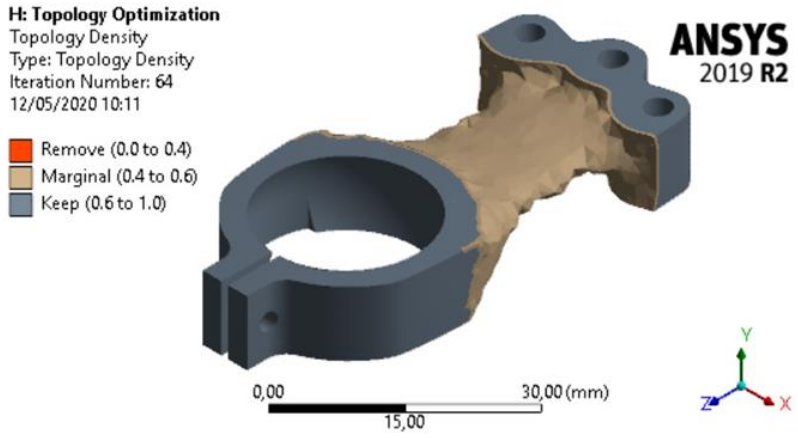

Figure 49. TO results of the level-ser based analysis.

Conversely, the results from the Density based solver were promising. In Figure 50 and Figure 51 can be seen the “minimum mass” and “maximum frequency” approaches, respectively, with the constraints informed on the beginning of this section. Both have similar geometries, with four arms going from the bolt area to the spherical joint. Based on these results, new geometries were generated, as in Figure 52. On different attempts, the arms thickness and height were varied (X and Y dimensions of Figure 53), to study which has the best grade with low enough stress values.

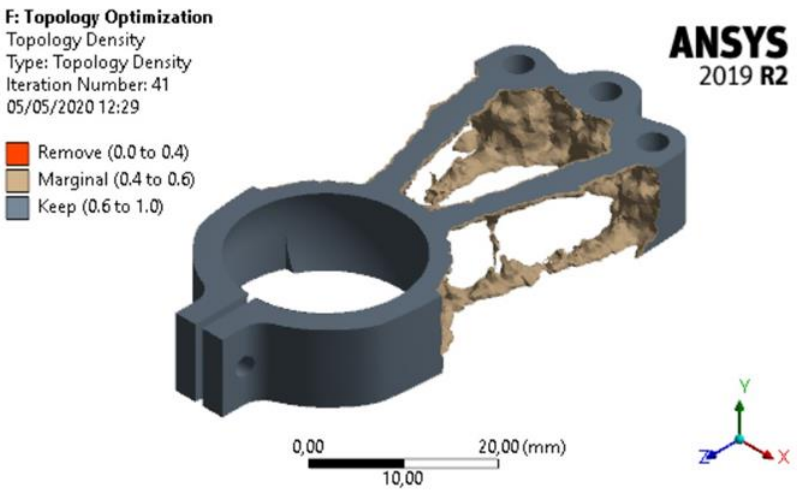

Figure 50. TO results of the density-based approach that has the goal of minimizing the mass while keeping the first natural frequency within a threshold.

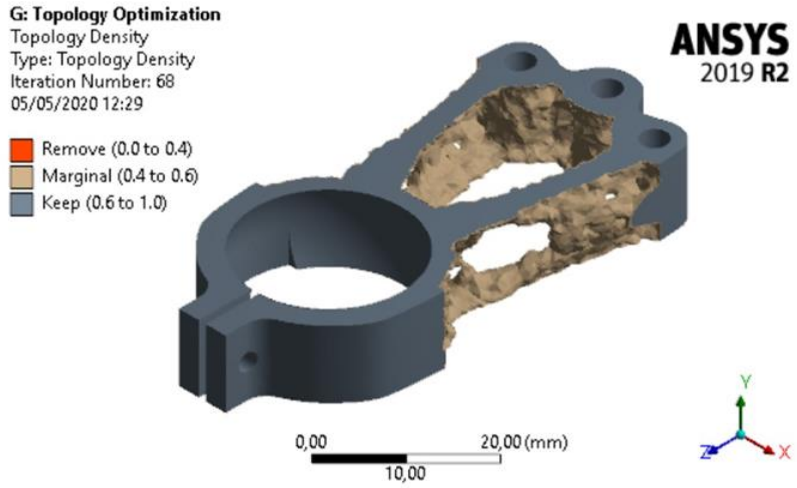

Figure 51. TO results of the density-based approach that has the goal of maximizing the frequency while keeping the mass within a threshold.

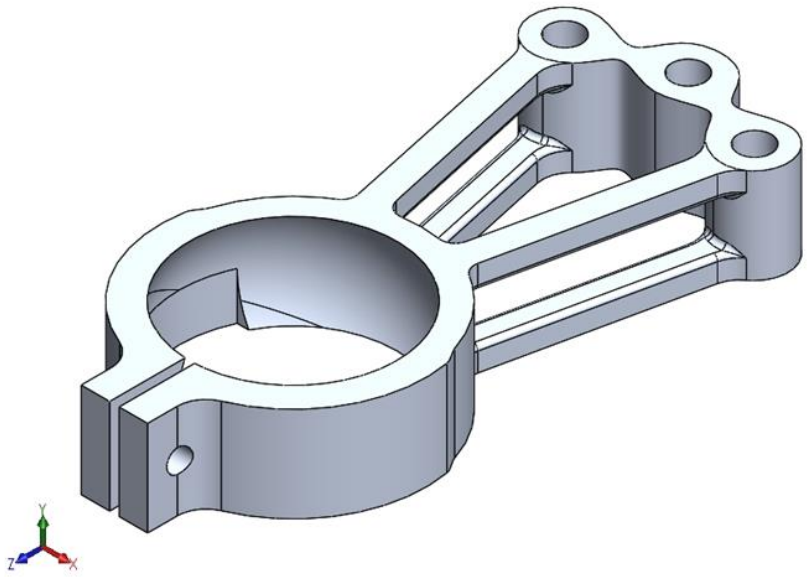

Figure 52. First model developed with the TO analysis results.

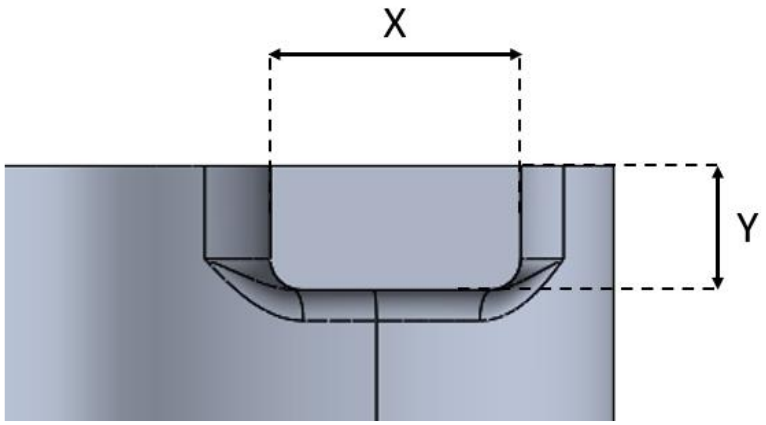

Figure 53. X and Y dimensions were varied in order to find the values that yield the best design grade.

From Table 13, it is concluded that the best geometry is the so called "Optimized model_thin_1", with X dimension of 2.77 mm and Y of 2.50 mm (same of Figure 52).

Name	Mass	1st nat.freq.	1st shape	2nd nat.freq.	2nd shape	3rd nat.freq.	3rd shape	GRADE
Optimized model	9.44 g	324 Hz	Torsion	419 Hz	Regular bending	1093 Hz	Middle bending	**2.55**
Optimized model_thick_1	9.83 g	315 Hz	Torsion	355 Hz	Regular bending	1024 Hz	Middle bending	**2.48**
Optimized model_thick_2	9.15 g	251 Hz	Torsion	299 Hz	Regular bending	958 Hz	Middle bending	**2.42**
Optimized model_thin_1	9.19 g	315 Hz	Torsion	420 Hz	Regular bending	1108 Hz	Middle bending	**2.57**
Optimized model_thin_2	8.74 g	265 Hz	Torsion	385 Hz	Regular bending	973 Hz	Middle bending	**2.53**

Table 13. Analysis table of the best models developed with the topology optimization method.

3.5.5 Lattice optimization models

3.5.5.1 Method explanation

Here, another ANSYS tool is used, the Lattice TO. This works in a similar way as the Density based TO but now it uses pre-generated materials (as on the Material Designer approach) calculated given a lattice shape, length and maximum/minimum volumetric material density (1 is a solid material, 0.5, for example, is a lattice with half of the element volume occupied and 0 is an empty region). The design, optimization region and symmetry constraints are the same as of section 3.5.4.1. However, here only the approach minimizing mass while setting a frequency constraint was used, with the first natural frequency set to be between 240-260 Hz.

From the possible lattice shapes that could be selected, only the "Octahedral 1" (same shape as the Diamond from section 3.5.3.1) attended the 45º overhang constraint. Then, for each lattice length (2 mm, 2.5 mm, 3.33 mm, 5 mm, and 10 mm), the minimum density to have 0.5 mm arm diameters was calculated. An example of the optimization input is on Table 14.

On this optimization, the solver changes the lattice element density (so, its arms diameter) throughout the model, resulting in a lattice that is non uniform and has higher densities in regions that influence more on the part's stiffness.

Optimization Type	Lattice Optimization
Lattice Type	Octahedral 1
Minimum Density	9,e-002
Maximum Density	1,
Lattice Cell Size	3,3333 mm

Table 14. ANSYS lattice optimization input options. The minimum arm diameter is determined by the minimum density value.

3.5.5.2 Results and comments

For a 3.33 mm lattice with minimum arms diameter of 0.5 mm, the results are inconclusive. As can be seen on Figure 54, the whole optimizable region has the minimum density, which indicates that the lattice is all with the 0.5 mm arm diameter, so, equal to the Diamond 3.33 mm case of section 3.5.3.1 but without the lateral 0.5 mm walls. As we know from the detailed simulations done previously, even with these lateral walls the initial stress was very high, thus, meaning this first lattice optimization result is not so valid. Similar results were obtained for 2 mm, 2.5 mm, 5 mm, and 10 mm lattice lengths.

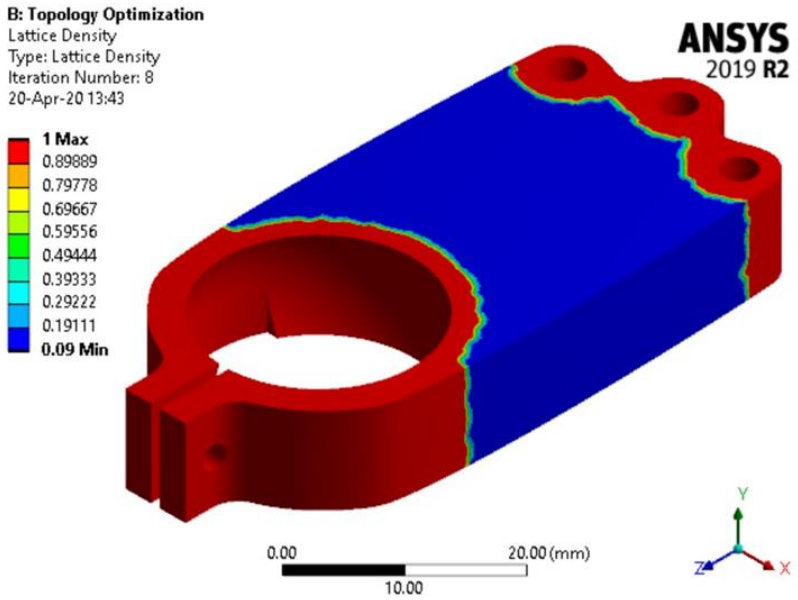

Figure 54. Lattice optimization done with diamond elements, 3.33 mm element size and minimum arm diameter of 0.5 mm.

After this, some trials were done reducing the minimum density to very low values, the equivalent of a 0.1 mm arm diameter (thus, would not be manufacturable). As can be seem on Figure 55, some of the section cuts along the model, show similar results to those obtained on the topology optimization analysis, further validating them.

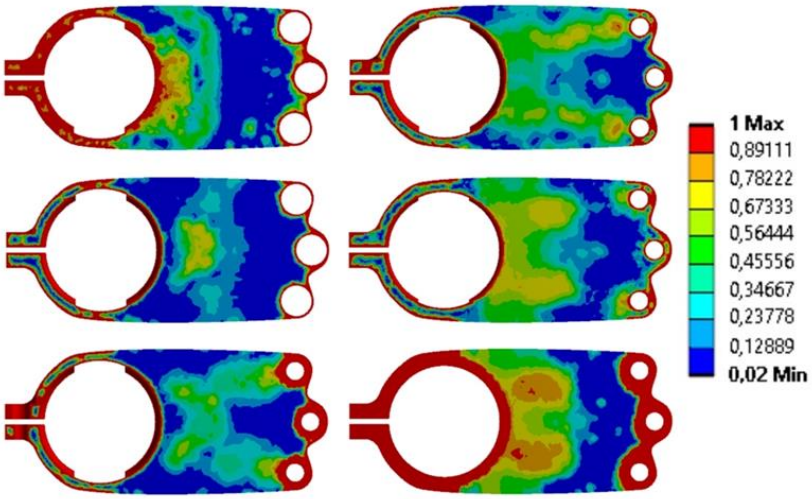

Figure 55. Lattice optimization done with diamond elements, 3.33 mm element size and minimum arm diameter of 0.1 mm. Each image is one layer of the model. The three on the right indicate similar results as those obtained in the TO analysis.

Apart from the inconclusive results, when generating the true lattice in ANSYS SpaceClaim software (regular post-processing software for this analysis), the resulting geometry is in a triangular mesh format, which was not properly turned into a final solid, even with huge efforts and time spent. Therefore, this method was unable to generate designs to be further compared.

3.5.6 External plate models

3.5.6.1 Method explanation

On this section, the pendulum arm is analyzed having just an external 0.5 mm thick plate around the walls and bottom of the optimizable region. Mathematically, it is known that material far from the geometric center axis is more influent on the moment of inertia of a beam than that near its center (The influence is proportional to the square of the distance between the material and the geometric center axis as seen on Figure 56). Thus, tests were done to study were the results with material the furthest away from the cross-section center while keeping its manufacturability by not having material on the top face. The first studied design is on Figure 57.

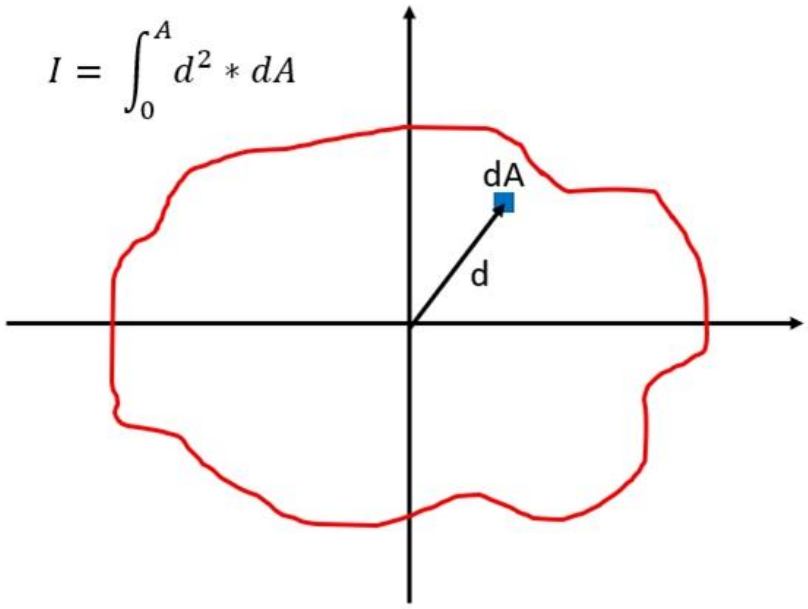

Figure 56. Representation of polar moment of inertia calculation. The reference axis is the one in the center.

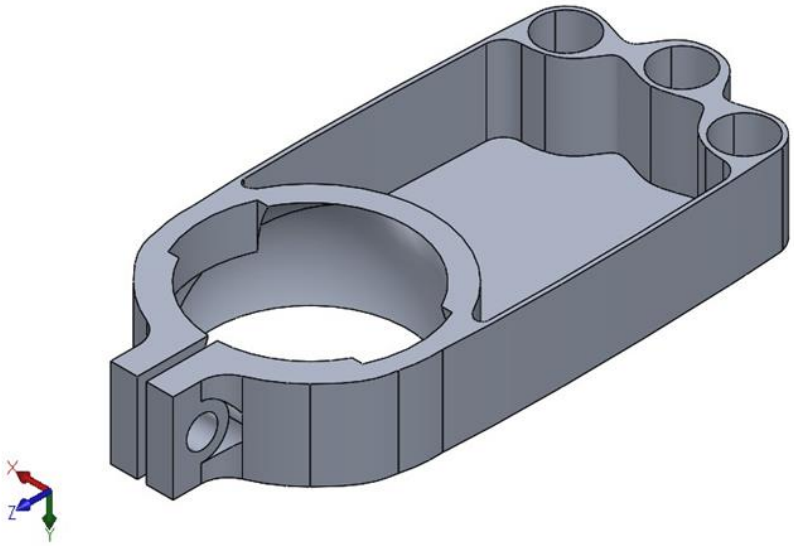

Figure 57. First design developed with the external plate method. Its section has the highest possible moment of inertia in all three axis. There is no upper plate because it would not be manufacturable by the AM process.

3.5.6.2 Results and comments

From the initial results of Table 16 can be concluded that the model can be further optimized since the first natural frequency and stresses are well inside the limit. Therefore, a TO was done, having as optimization region the blue region in Figure 58. All parameters were the same used in section 3.5.4.1 but the Y symmetry constraint was removed, since we don't want material in the top part here and an overhang constraint of 45º was added (to avoid as much as possible any overhangs).

Name	Mass	1st nat.freq.	1st shape	2nd nat.freq.	2nd shape	3rd nat.freq.	3rd shape	GRADE	Stress
Plate	9.66 g	414 Hz	Regular bending	646 Hz	Torsion	1524 Hz	Middle bending	**2.57**	115 MPa

Table 15. Analysis table of the first model developed with the external plate method.

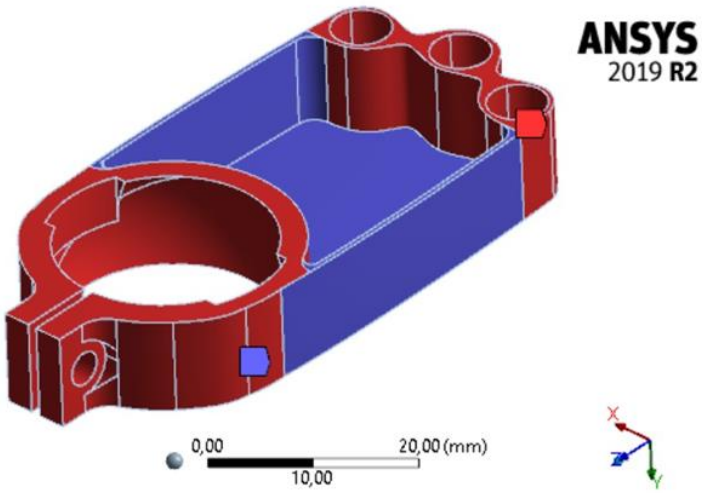

Figure 58. Design region (blue) and exclusion region (red) used in the TO for the external plate method.

The results of Figure 59 indicate a complex geometry, which after multiple design iterations was simplified to the design in Figure 60. Table 16 shows that this has a better grade than all other structures previously analyzed while also having no need for overhang supports on its manufacture.

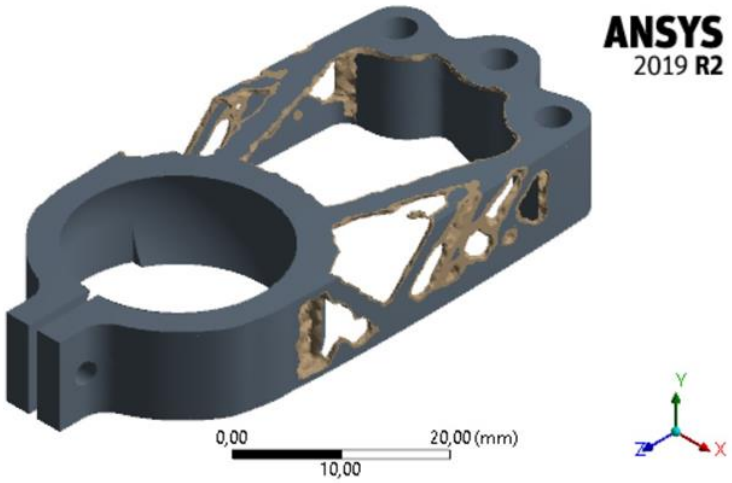

Figure 59. External plate TO result.

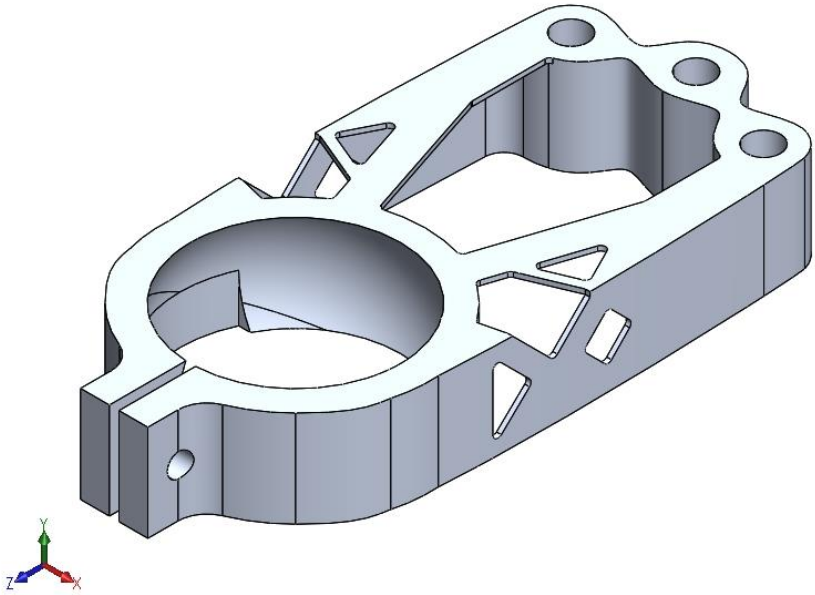

Figure 60. Model generated by the result obtained in the TO.

Name	Mass	1st nat.freq.	1st shape	2nd nat.freq.	2nd shape	3rd nat.freq.	3rd shape	GRADE	Stress
Plate_opt_3	8.90 g	337 Hz	Regular bending	493 Hz	Torsion	897 Hz	Lateral bending	**2.63**	135 MPa

Table 16. Analysis table of the best models developed with the external plate method.

3.5.7 Comparison of the results and discussion

As can be seen on Table 17, the best results from each method were all much better than the previous pendulum arm design. From the four best, the last two, "Optimized model_thin_1" and "Plate_opt_3" were those used on the more detailed stress analysis, with load multiple directions and stress convergence analysis with the mesh.

The lattice models were initially expected to have the best results among all, however, the constraints on lattice arm diameter and the inability to use better lattice shapes may have been the turning point on this aspect.

It is curious that the basic TO found results worse than the TO done just with an external plate. Probably because the solver found a local minimum and not a global minimum, which was that of the external plate TO (or even there are better shapes not found by the program in either case).

Name	Mass	1st nat.freq.	1st shape	2nd nat.freq.	2nd shape	3rd nat.freq.	3rd shape	GRADE	Stress
Previous design	14.60 g	489 Hz	Regular bending	899 Hz	Torsion	2303 Hz	Middle bending	**1.99**	37 MPa
Honeycomb 11mm_final	10.51 g	377 Hz	Regular bending	505 Hz	Lateral Bending	1285 Hz	Torsion	**2.44**	183 MPa
Diamond 3.33mm_lat	9.83 g	316 Hz	Lateral Bending	328 Hz	Regular bending	890 Hz	Torsion	**2.43**	159 MPa
Optimized model_thin_1	9.19 g	315 Hz	Torsion	420 Hz	Regular bending	1108 Hz	Middle bending	**2.57**	192 MPa
Plate_opt_3	8.90 g	337 Hz	Regular bending	493 Hz	Torsion	897 Hz	Lateral bending	**2.63**	135 MPa

Table 17. Analysis table of the best models overall and the previous design.

For the stress convergence, the mesh was refined initially with the ANSYS Mechanical "refinement" feature [58] with a refinement level of two applied to all faces on the optimizable region. This resource changes the elements in a surface to have better shapes (in our case, closer to a regular triangle), thus, reducing the elements size. Then, if the stresses found are higher than the threshold, more model changes are done to reduce it. After these changes, local refining using mesh element size was done on the most stressed region, to study to which value it converges. Convergence was analyzed according to the fit below, which was found to be the best for the values encountered.

$$Stress = A + (B - A)/(1 + (ElementSize/C)^D)$$

3.5.7.1 Topology optimization model refinement

For the initially refined mesh on the TO best model, the maximum stress was higher than the minimum, its value is 236 MPa for the +Y direction acceleration (worse load case). It is shown is in Figure 61.

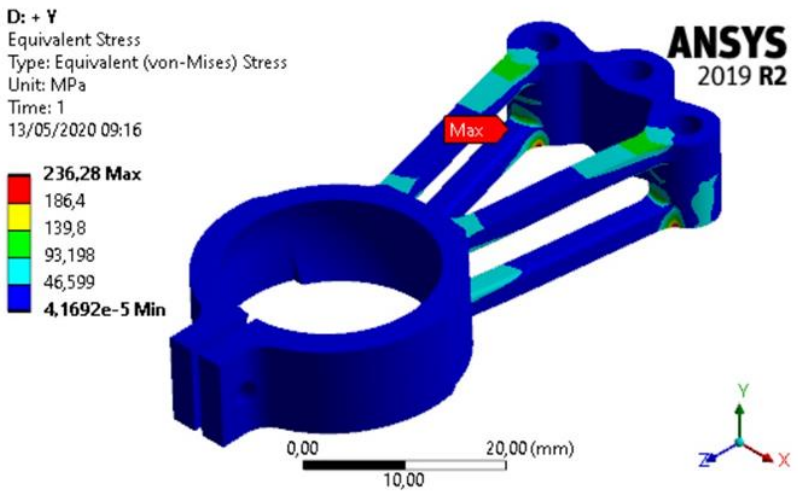

Figure 61. Stress plot for the TO analysis model with refined mesh.

This required model changes at the most stressed region. Each of the arms height (Y dimension in Figure 53) was kept unchanged but a new profile was used on their thickness. The geometry is on Figure 62. Since stress in the middle of the arms was very low (order of 30 MPa), the thickness on the center was reduced from 2.5 mm to 2 mm. With this change, the maximum stress reduced to 140 MPa with acceleration on the +X -Y direction. Thus, this will be the load direction used on the stress convergence.

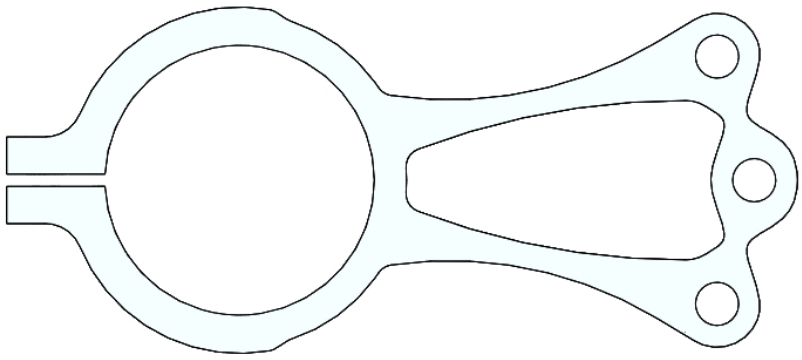

Figure 62. New model developed to reduce the maximum stress on the TO model.

According to Figure 63, it converges to 150 MPa, this is considered the maximum stress for the topology optimization final design. The most stressed region is in Figure 64 and the final model is in Figure 65.

Element size	Stress
0.50 mm	126 MPa
0.30 mm	130 MPa
0.20 mm	142 MPa
0.15 mm	143 MPa
0.10 mm	145 MPa
0.05 mm	150 MPa
0.03 mm	150 MPa
0.01 mm	151 MPa

Table 18. Stress values for each mesh element size of the TO method stress convergence.

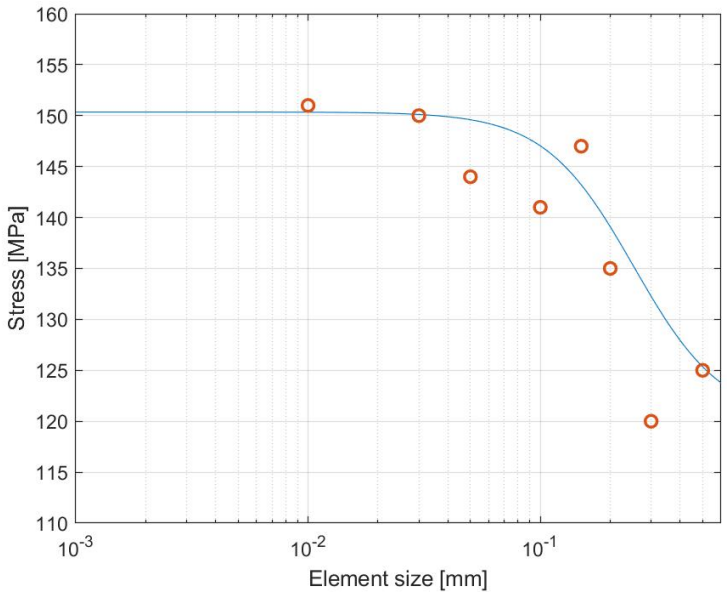

Figure 63. Plot of the stress convergence fit (blue line) of the TO method.

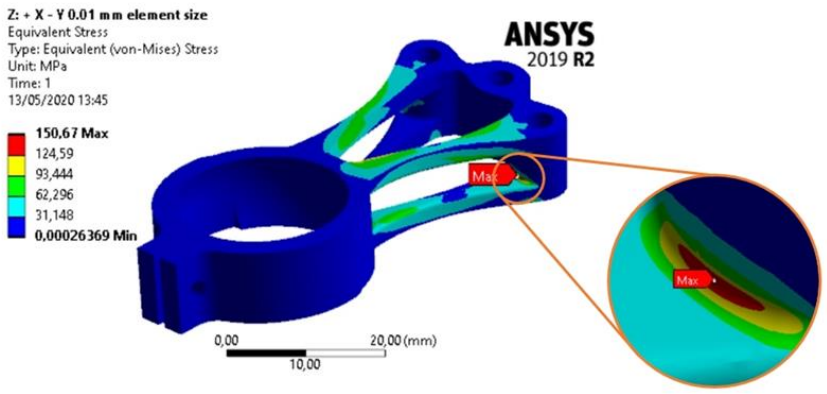

Figure 64. Zoom of the region where the stress is maximum at the TO method analysis.

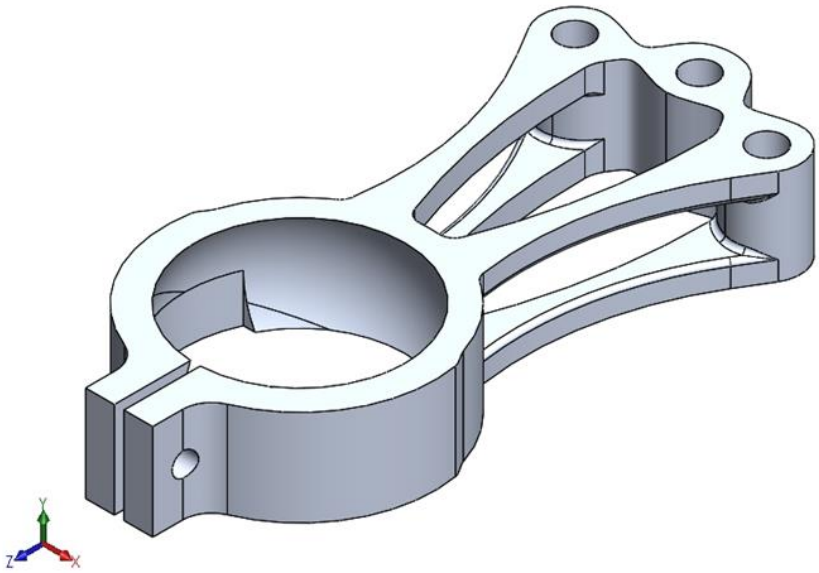

Figure 65. Final geometry of the model developed with the TO method.

Name	Mass	1st nat.freq.	1st shape	2nd nat.freq.	2nd shape	3rd nat.freq.	3rd shape	GRADE	Stress
Final_TO	9.32 g	316 Hz	Torsion	466 Hz	Regular bending	1196 Hz	Middle bending	**2.55**	150 MPa

Table 19. Analysis table of the final model of the TO method.

3.5.7.2 External plate model refinement

For the “Plate_opt_3”, the maximum stress (obtained at +Y direction) after the mesh was refined jumped to 230 MPa, around its triangular lateral cut and 200 MPa on top of one of its walls. This is shown in Figure 66.

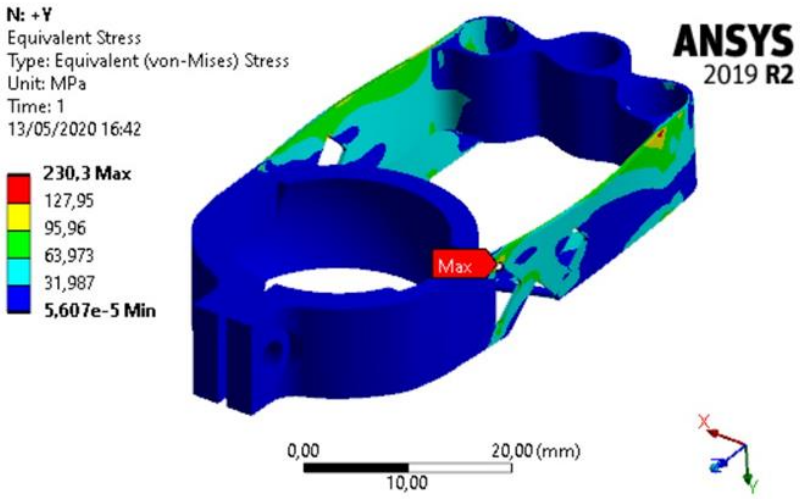

Figure 66. Stress plot for the external plate model with refined mesh.

Then, the model was changed in an iterative procedure, which more than eight different trials were done and the maximum stress (acceleration at +X -Y direction) reduced to 138 MPa. Mainly, the top bars were enlarged, and the side walls thickness was increased. This model is on Figure 67 and it will be used for the stress convergence, with load at +X -Y direction.

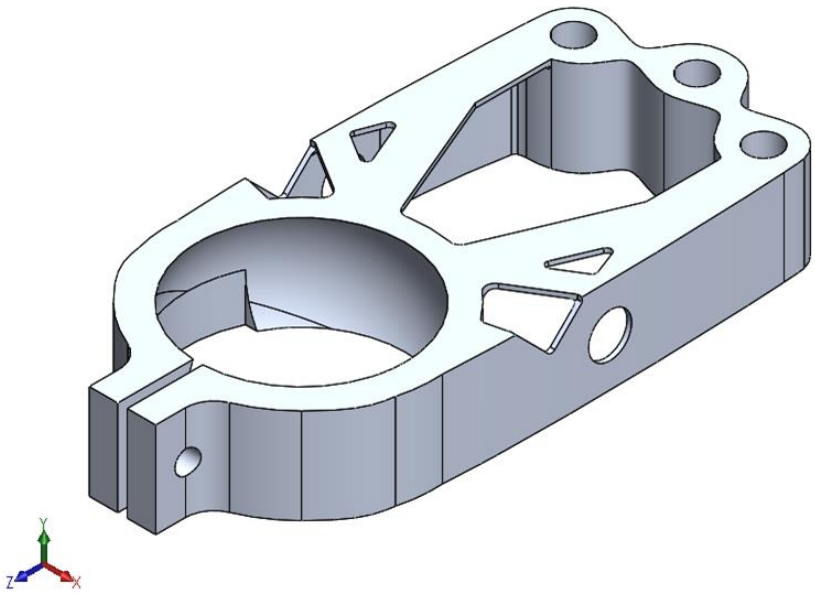

Figure 67. Final geometry of the model developed with the external plate method.

On the convergence fit, the 0.50 mm and 0.15 mm elements were disregarded due to their behavior. Figure 68 indicates that it converges to 146 MPa (uses same convergence fit of section 3.5.7). The most stressed region is in Figure 69 and the final model is that of Figure 67.

Element size	Stress
0.50 mm	125 MPa
0.30 mm	120 MPa
0.20 mm	135 MPa
0.15 mm	147 MPa
0.10 mm	141 MPa
0.05 mm	144 MPa
0.03 mm	145 MPa
0.01 mm	146 MPa
0.08 mm	146 MPa

Table 20. Stress values for each mesh element size e of the external plate method stress convergence.

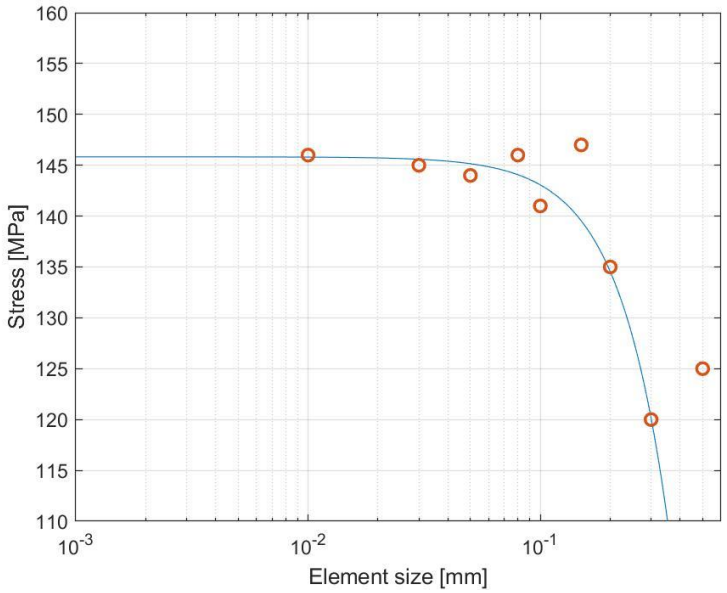

Figure 68. Plot of the stress convergence fit (blue line) of the external plate method.

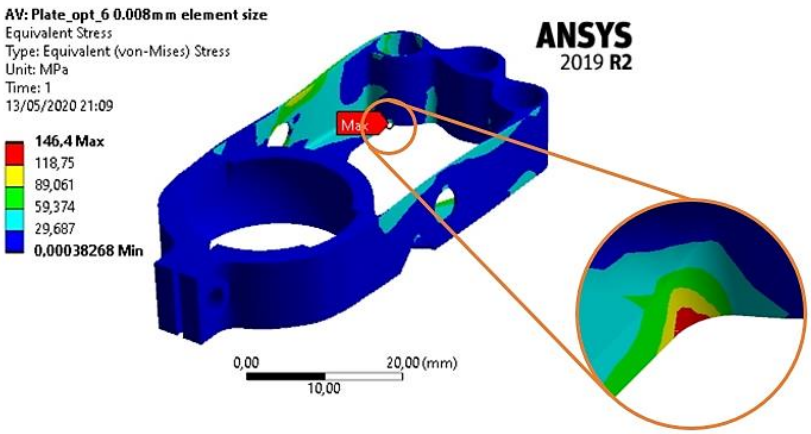

Figure 69. Zoom of the region where the stress is maximum at the external plate method analysis.

Name	Mass	1st nat.freq.	1st shape	2nd nat.freq.	2nd shape	3rd nat.freq.	3rd shape	GRADE	Stress
Final_plate	9.16 g	368 Hz	Regular bending	546 Hz	Torsion	1000 Hz	Lateral Bending	**2.62**	146 MPa

Table 21. Analysis table of the final model of the external plate method.

4 Double pendulum arm

4.1 Introduction

On this section, there is a redesign of the shaft connection and pendulum arms (cyan and yellow regions of Figure 70) to be a single piece. This has many benefits, such as significant weight reduction and removal of many fasteners. However, as will be seen, new problems arise. For this analysis, the only method used is the density-based topology optimization. Below there will be the description of the method used, results and new issues.

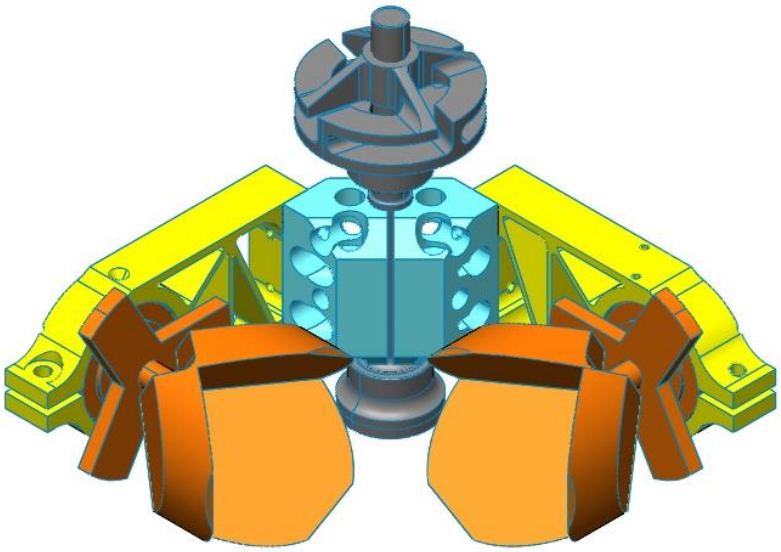

Figure 70. Mirror (orange) + Pendulum Arms (yellow) +Shaft connection (cyan) + Shaft (grey).

4.2 Design constraints and optimization region

As done for the single pendulum arm, first is defined the region to be optimized. This is the grey region of Figure 71 and Figure 72, and it consists of the available region, where no other MIMA components are present, it was extracted from the MIMA assembly (Figure 2). The pendulum tips (yellow part of the figures below) are maintained as before to keep the same CCM alignment properties. Therefore, the optimization region does not include them.

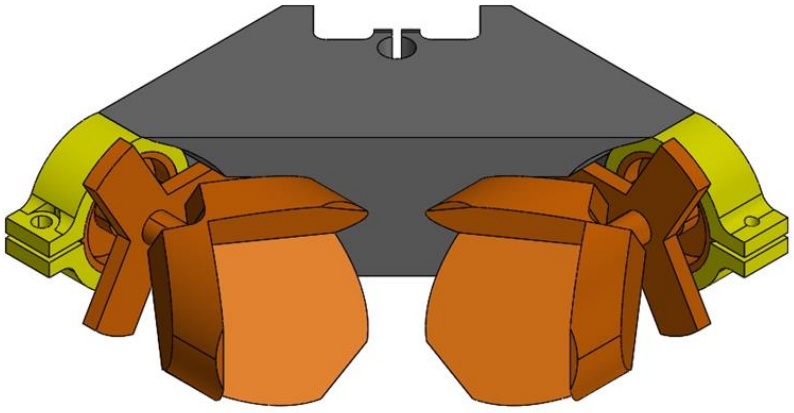

Figure 71. Region to be optimized (grey) + Pendulum tips (yellow) + Mirror (orange). View 1.

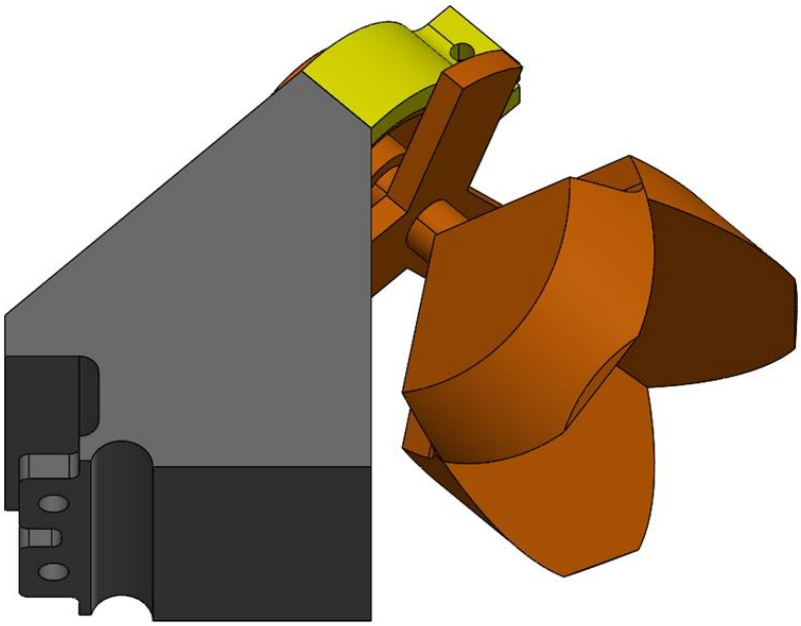

Figure 72. Region to be optimized (grey) + Pendulum tips (yellow) + Mirror (orange). View 2.

4.3 FEA Model

4.3.1 Constraints and their equivalent on the FEA model (boundary conditions)

On this case there is only one constraint, located on the connection of the shaft to the part to be designed. It was used a fixed support because all 6 dofs are constrained, this is detailed in Figure 73. Also, as a simplification, the tip of the pendulums and CCMs together were substituted by a point mass representing their mass/inertia and was connected to the region where the tip of the pendulum had contact with the optimization region (Figure 74).

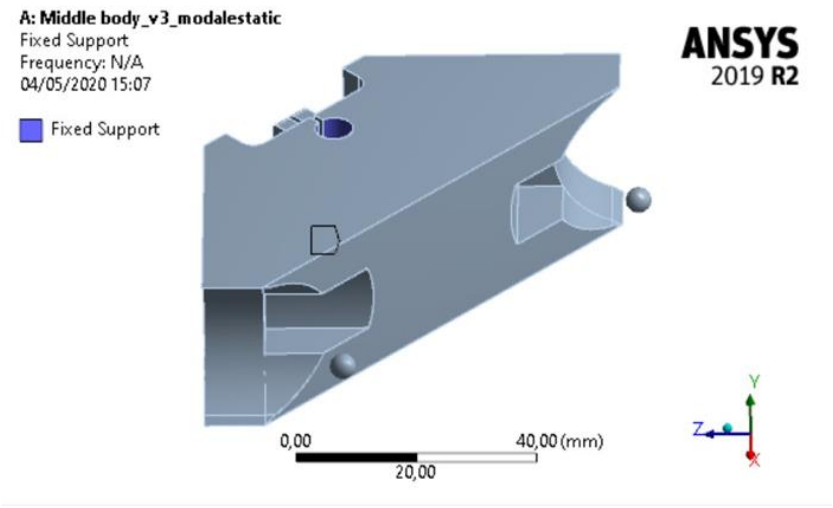

Figure 73. Fixed support boundary condition (region in blue).

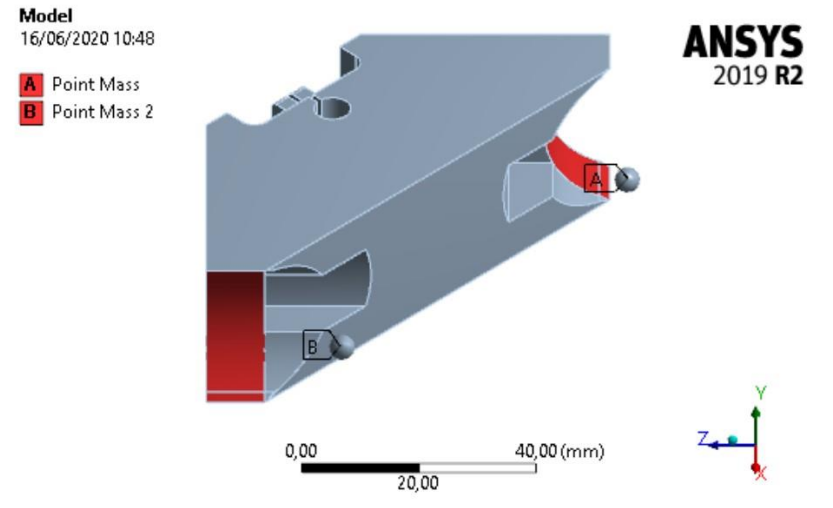

Figure 74. Two "point mass" are present (spheres A and B) and are connected to the surfaces where the pendulum tips has contact with the optimizable region (red surfaces).

4.3.2 Mesh

The premises for meshing were the same as those of the single pendulum design. It was also used ANSYS adaptative sizing with the highest possible resolution, generating tetragonal elements refined on the edges based on curvature and proximity [58]. For more information, look at section 3.4.2. Figure 75 is a representation of how the final mesh was.

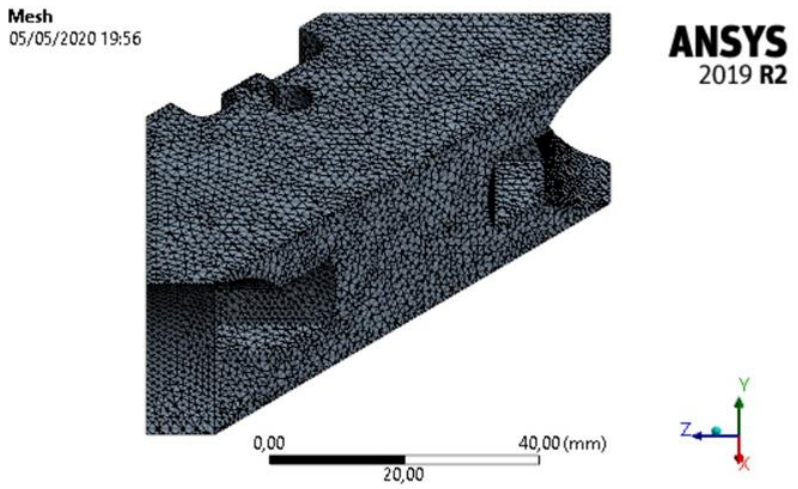

Figure 75. Surface mesh on the double pendulum model.

4.4 Analysis

4.4.1 Analysis input

Differently from the single pendulum, for this analysis was used only density-based topology optimization. This problem is much more geometrically complex, then, it is not straightforward to apply the same principles as before to try to achieve different results.

The TO here had always as objective maximizing the first natural frequency, so, a constraint was set to the mass. For this were used 7%, 10%, 15%, 20%, 25% and 30% of the original mass value. Besides, an acceleration load with the design load's magnitude (1386 m/s²) was applied on the +X +Y direction together with a constraint of maximum Equivalent Von Mises stress of 203 MPa (Yield strength of the stress relieved AlSi10Mg). Therefore, it was a maximization problem with one equality (percentage of the original mass value) and one inequality (maximum equivalent Von Mises stress) constraint. Apart from these, two symmetry constraint planes were set, as on Figure 76 and Figure 77.

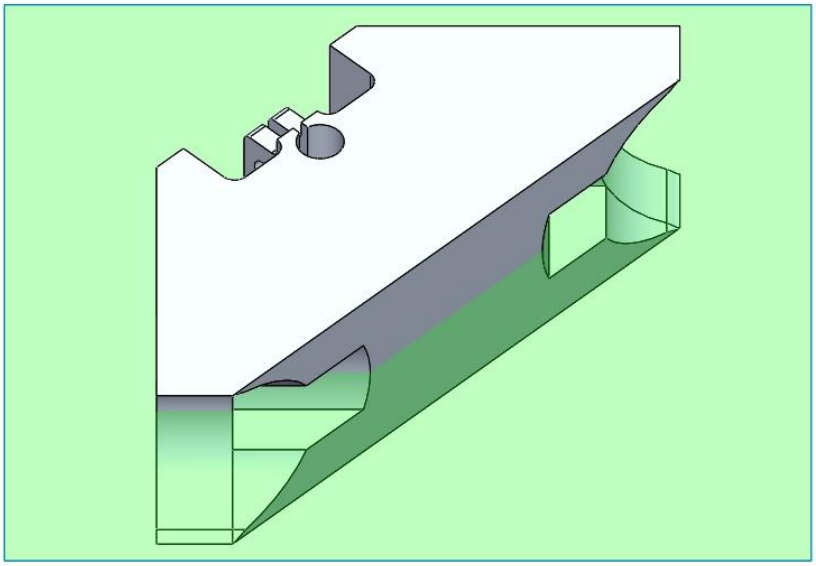

Figure 76. Vertical symmetry constraint on the double pendulum model.

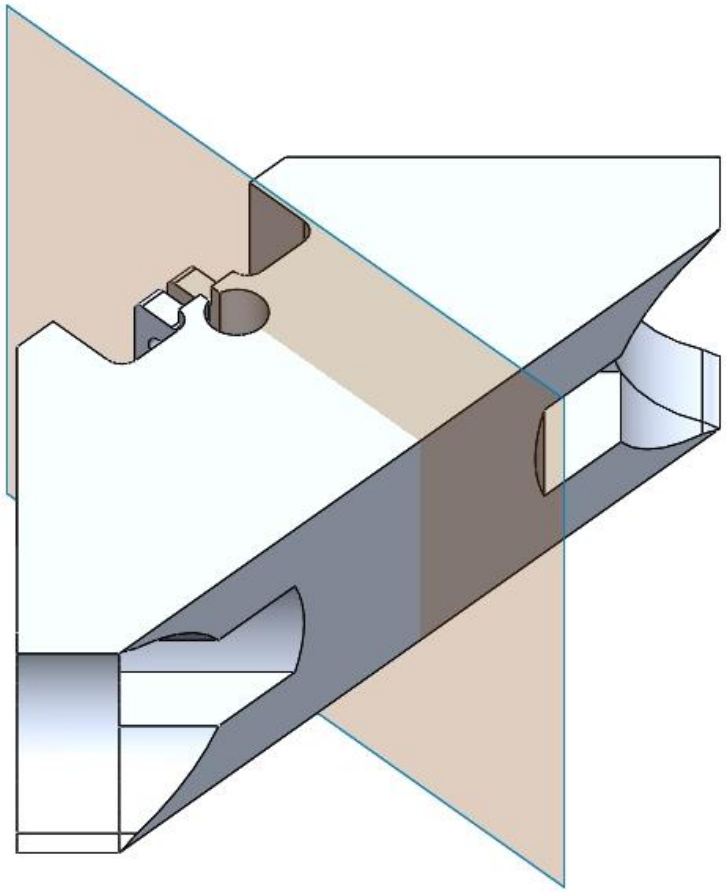

Figure 77. Horizontal symmetry constraint on the double pendulum model.

4.4.2 Initial results and further development

All the different mass constraint simulations gave similar overall shapes. It has mass only on the outer parts of the optimizable region and some specific geometries on the top and laterals. Figure 78 shows the result for an optimization objective of 10% of the original mass and Figure 79, of 15% of the original mass. The 10% case, for example, had its first natural frequency at 355 Hz, well above the minimum of 200 Hz.

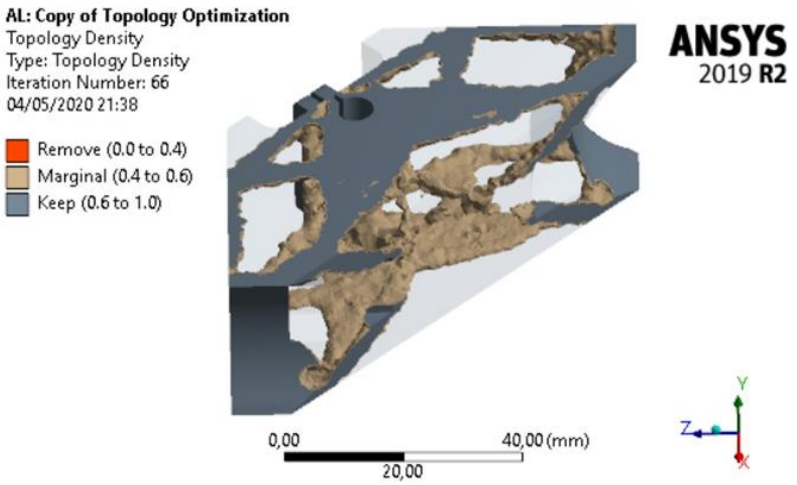

Figure 78. TO results for 10% of the original mass and maximum possible first natural frequency.

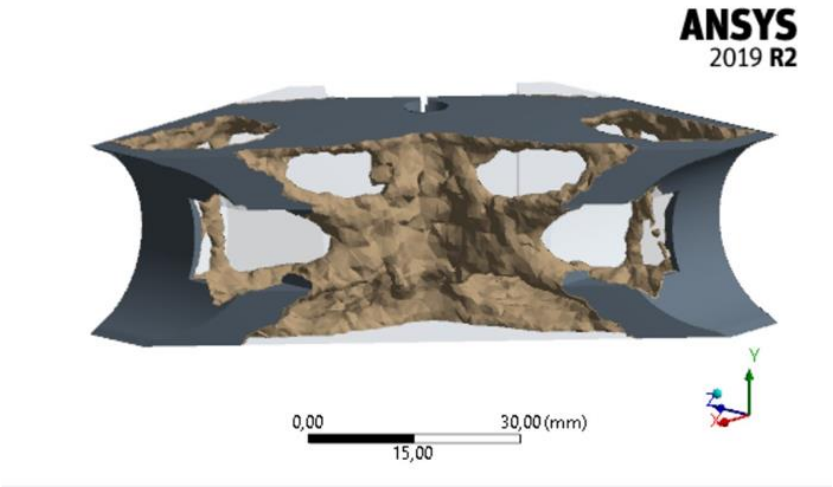

Figure 79. TO results for 15% of the original mass and maximum possible first natural frequency.

By these results the model of Figure 80 was created. An analysis of it with the same boundary conditions as the optimizations gave a first natural frequency of 770 Hz and maximum stress of 110 MPa, both far from the limit values (minimum first natural frequency of 200 Hz and maximum stress of 203 MPa). This means that this model can be further changed so a more optimized shape (lower mass) is found. Its current mass is of 34.87 g.

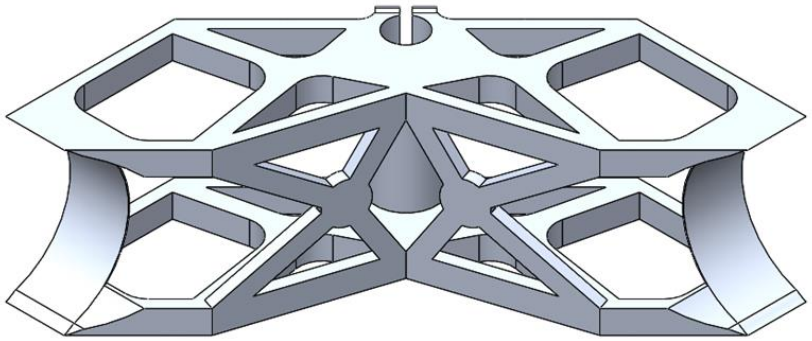

Figure 80. Initial double pendulum model developed with the TO results.

4.4.3 Further iterative optimization to find a suitable model.

The first model was iteratively changed to reach the final. The procedure used was to analyze the regions with most displacement from the first three mode shapes and change them, increasing the stiffness (more trusses, increased thickness) when the natural frequency is below the minimum and vice versa when it is above the minimum. All designs are in Figure 81, Figure 82 and Figure 83.

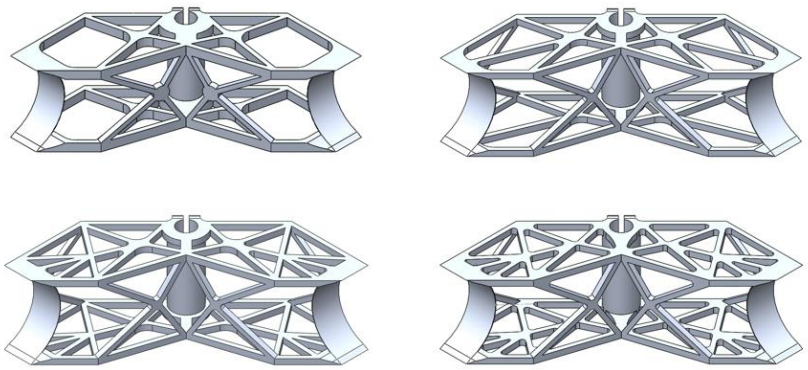

Figure 81. Iterative optimization of the initial shape. 1) Top-left; 2) Top-right; 3) Bottom-left; 4) Bottom-right.

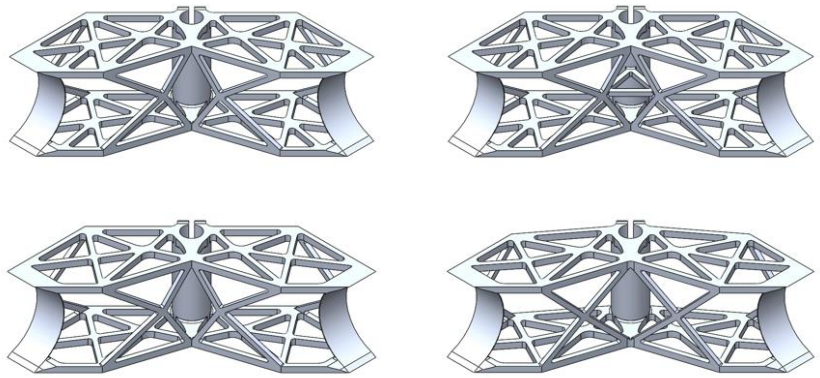

Figure 82. Iterative optimization of the initial shape. 5) Top-left; 6) Top-right; 7) Bottom-left; 8) Bottom-right.

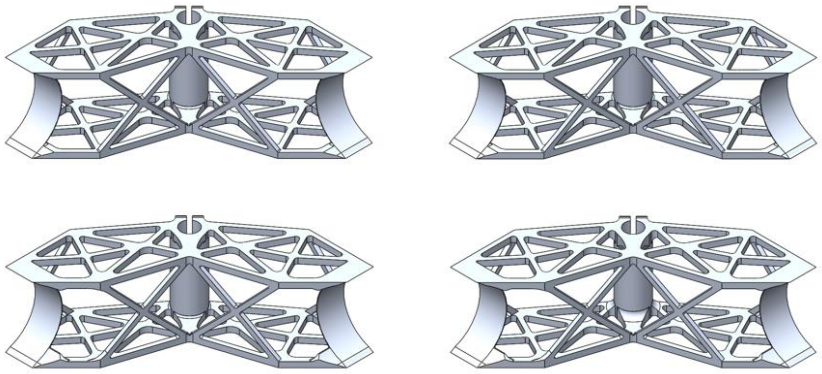

Figure 83. Iterative optimization of the initial shape. 9) Top-left; 10) Top-right; 11) Bottom-left; 12) Bottom-right.

The last version is on Figure 84 and Figure 85. The mass is of 25.60 g, much lower than the original mass of the equivalent components (around 70.00 g, the cyan and yellow parts of Figure 70), not considering the fasteners that reduced from ten to just four.

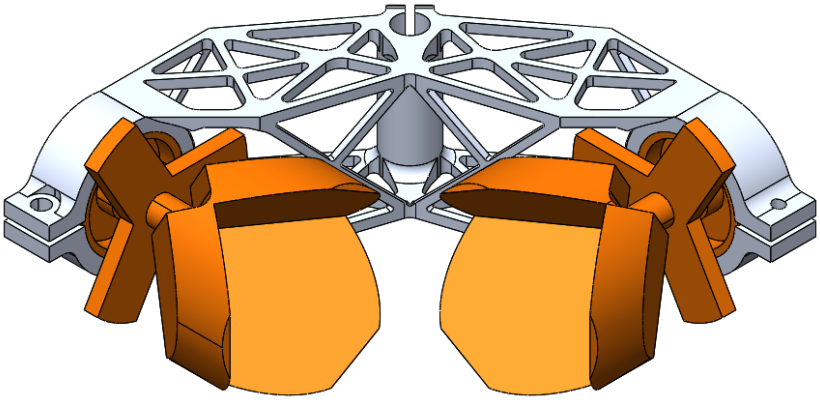

Figure 84. Final optimized version of the double pendulum design. View 1.

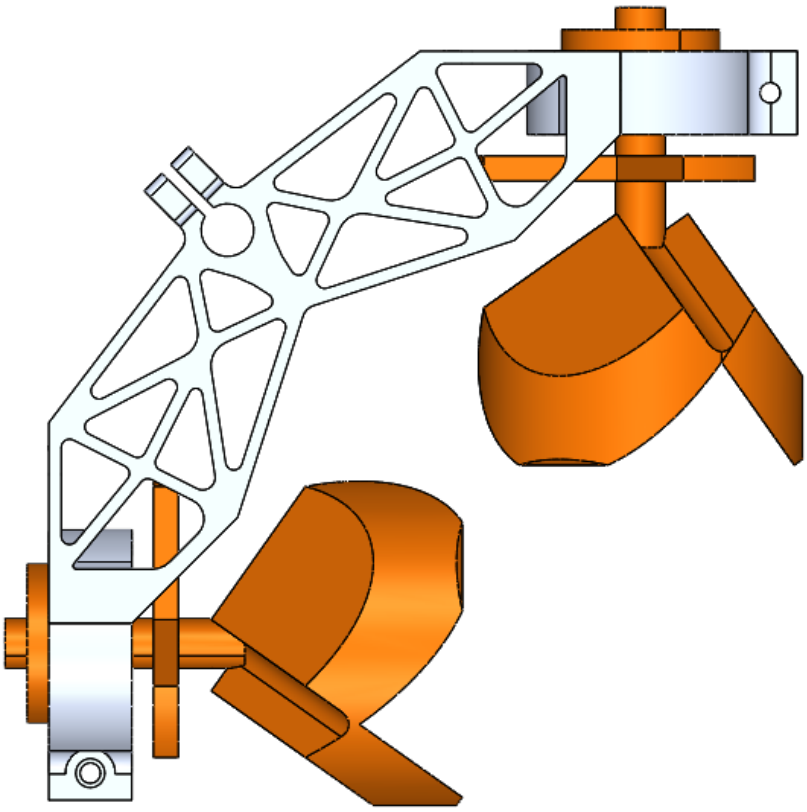

Figure 85. Final optimized version of the double pendulum design. View 2.

The natural frequencies are shown on Table 22. Indeed, they are still much higher than the minimum required but this is seen as positive because of the extra safety. Also, the first three natural frequencies are very close, and this is also positive because means that the stiffness was well distributed during the iterative process among these three modes.

Mode #	Frequency
1	445 Hz
2	473 Hz
3	476 Hz
4	704 Hz
5	732 Hz
6	878 Hz

Table 22. Natural frequencies of the final double pendulum design.

From this last model the 1386 m/s² acceleration was applied in all axis and axis combinations. The maximum stress was found for the +X +Z direction (Figure 86) and was initially of 123 MPa. A stress convergence study was done on the region where the maximum was obtained. It indicates that the stress converges to 126 MPa (used same convergence fit as section 3.5.7), a value well below the limit of 203 MPa. Therefore, this model is considered to be very successful in keeping decent performance while greatly reducing the total mass.

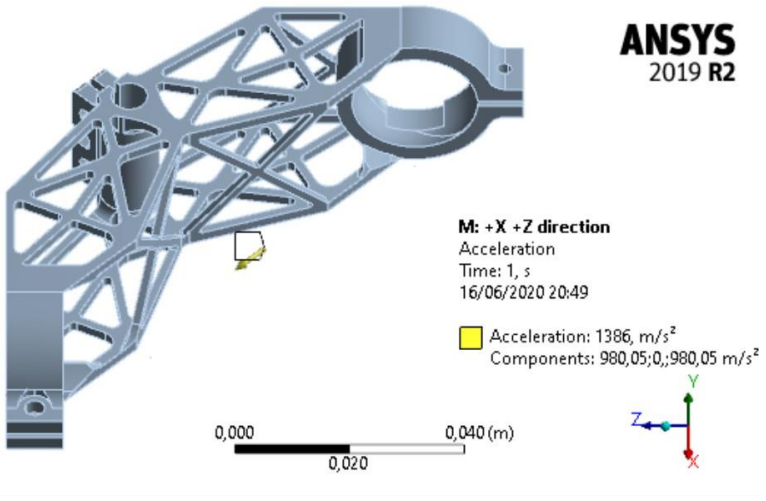

Figure 86. Acceleration direction (+X +Z) that yields the highest stress on the part.

Element size	Stress
2.00 mm	112 MPa
1.00 mm	115 MPa
0.50 mm	116 MPa
0.30 mm	122 MPa
0.15 mm	124 MPa
0.05 mm	126 MPa
0.03 mm	126 MPa
0.01 mm	125 MPa
0.05 mm	125 MPa

Table 23. Stress values for each mesh element size of the double pendulum stress convergence.

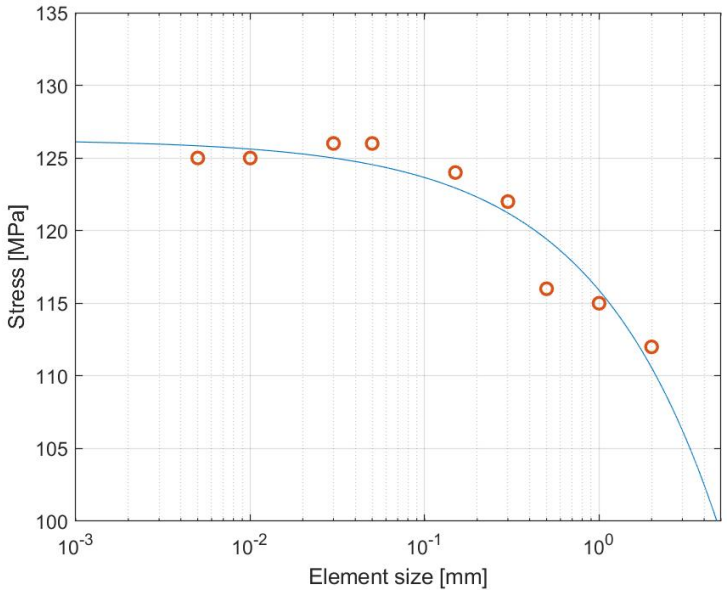

Figure 87. Plot of the stress convergence fit (blue line) of the double pendulum model analysis.

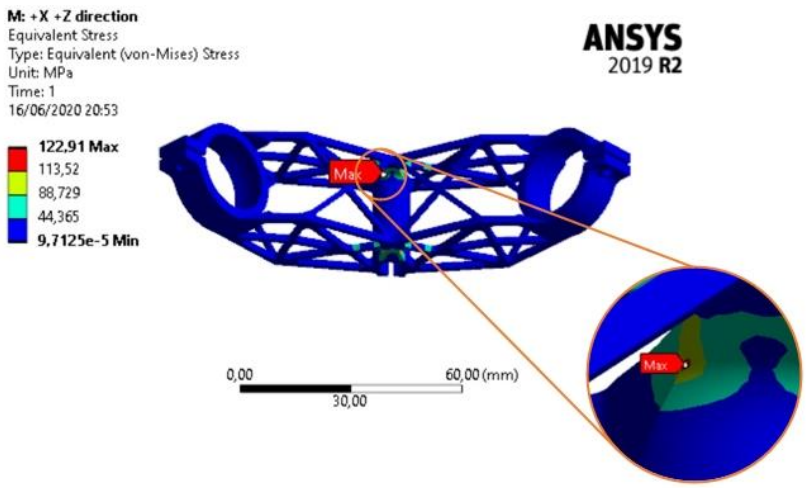

Figure 88. Zoom of the region where the stress is maximum at the double pendulum model analysis.

4.5 Further required analysis

However, even it being a success in performance, there are two new challenges to be overcome. Firstly, the fixation system must keep the part still when the maximum acceleration is applied, and secondly it must be done in such way that the tightening of the bolts does not displace the mirrors more than one micrometer, otherwise the spectrometer's accuracy is ruined.

4.5.1 Fixation system compliance

For guaranteeing the part is kept still, the first step is to calculate the torque and the vertical force acting on the fixation area when it is subject to accelerations from different directions, as shown in Figure 89. This can be done in an ANSYS analysis by measuring the reaction force and torque at the fixed support boundary condition when the part is subject to an acceleration. Note that the normal force at the shaft-double pendulum interface due to lateral force was disregarded, therefore all normal force from the piece at the axle comes from the bolts' forces.

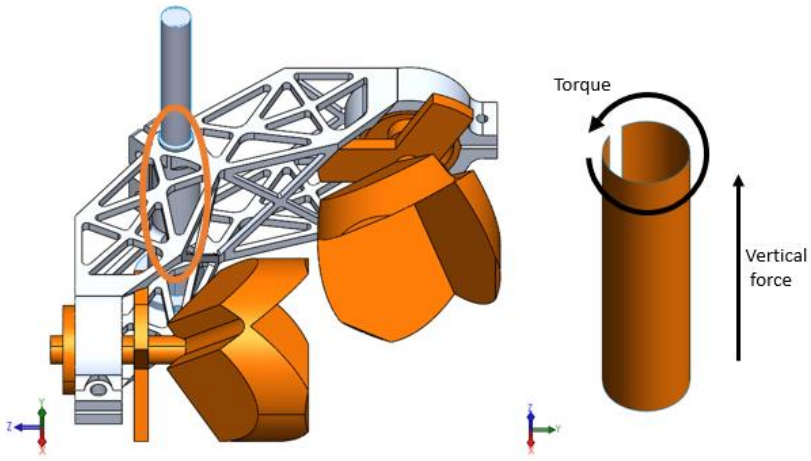

Figure 89. In orange on the left is the region where the shaft has contact with the double pendulum model. On the right is a representation of the torque and vertical forces measured at the ANSYS analysis.

Having these two values for different acceleration inputs, is possible to calculate a resultant tangential force that acts on the fixation area by the formula below. The highest resultant force is for the acceleration at the +X +Z direction and has a magnitude of 1434 N. Then, considering a static friction coefficient of 1.05 for aluminum-aluminum interface [60], the total clamping force that must be granted by the bolts is 869 N.

$$F_{tangential} = \sqrt{(F_{vertical})^2 + \left(\frac{Torque}{radius}\right)^2} \qquad F_{total} = \frac{2 * F_{tangential}}{1.05 * \pi}$$

Therefore, since there are two bolts, each must withstand a force of 434.5 N. On the previous pendulum arm design were used M3 A2-70 stainless steel bolts which withstand up to 1360 N [61] of traction force. Considering that each bolt will be tightened up to 1.5*434.5 = 651.75 N for safety, a stress analysis study was done to validate the designed bolt fixations.

The model is described on Figure 90, a force of 651.75 N was applied to the bolts head/nut and a fixed support was set where the part has contact with the shaft. The maximum stress obtained converged to 126 MPa (used same convergence fit as section 3.5.7), well inside the limit of 203 MPa. Table 24 has the convergence values and Figure 91, the plot. According to Figure 92, the maximum stress is of 207 MPa, but this was at the boundary condition and considered to be not valid, thus being disregarded.

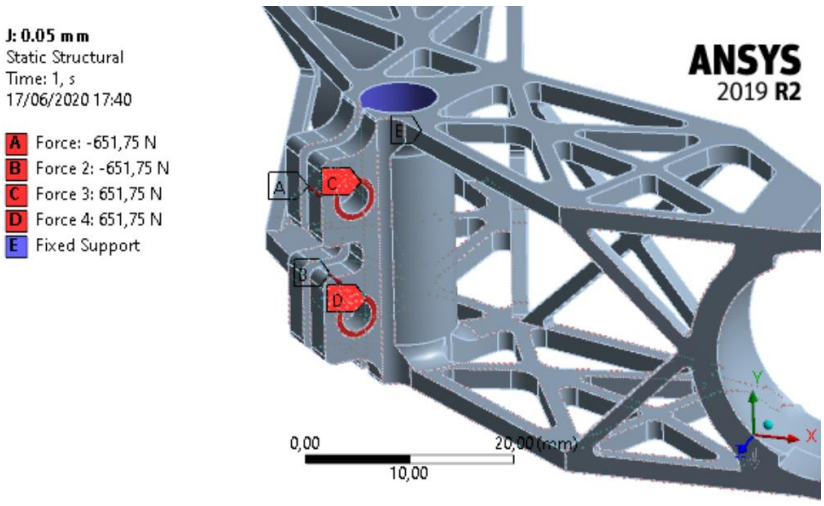

Figure 90. ANSYS model to find the stress at the part when the bolts are tightened.

Element size	Stress
1.00 mm	112 MPa
0.50 mm	115 MPa
0.30 mm	120 MPa
0.15 mm	121 MPa
0.05 mm	125 MPa
0.03 mm	125 MPa
0.01 mm	126 MPa

Table 24. Stress values for each mesh element size of the bolt force analysis stress convergence.

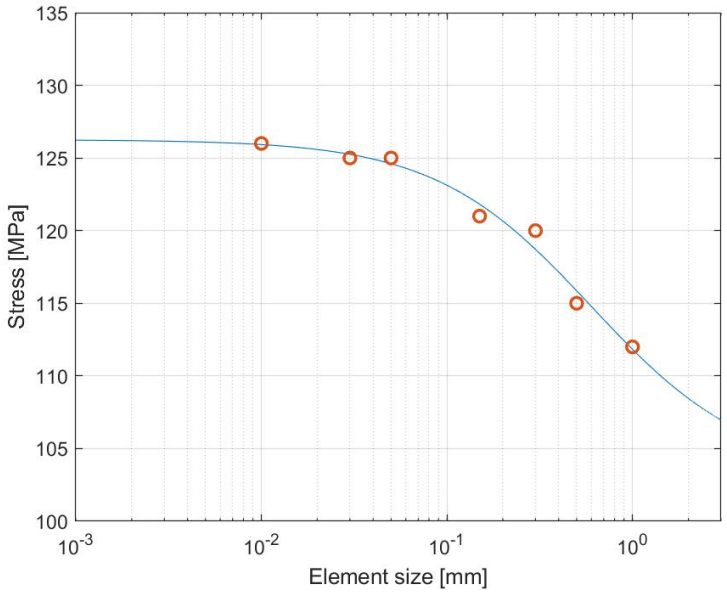

Figure 91. Plot of the stress convergence fit (blue line) of the bolt force analysis.

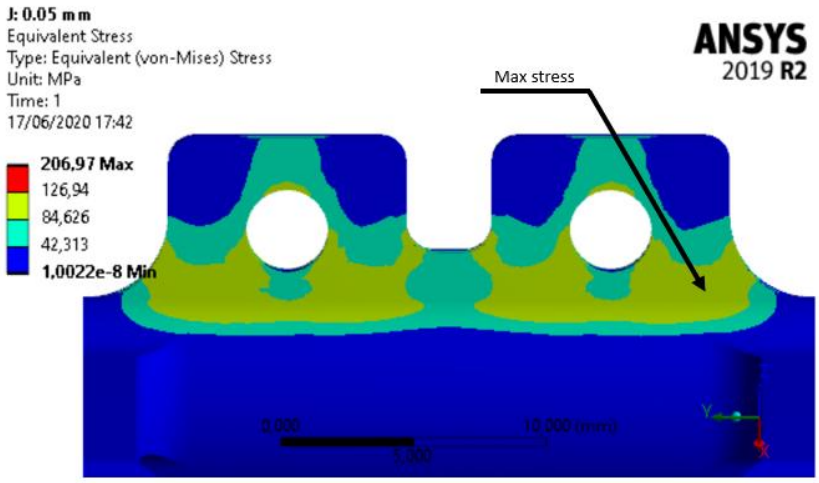

Figure 92. Stress plot at the bolt fixations when the bolt forces are applied.

4.5.2 Mirror displacement

On the analysis to guarantee the displacement on the center of the CCM is below 1 micrometer, a displacement input is applied at the bolt fixations around the shaft hole, up until it reaches the shaft diameter. It was considered that the shaft hole of the part is manufactured with its diameter 0.1 mm bigger than that of the shaft, so, the displacement required to reduce the diameter by this amount is $0.1*\pi = 0.314$ mm. Therefore, each of the two sides of the bolt fixations is displaced by $0.314/2 = 0.157$ mm. The analysis input is as detailed on Figure 93, and, apart from this displacement indicated by the arrows, the two surfaces in yellow have the Y axis and Z axis movement constrained.

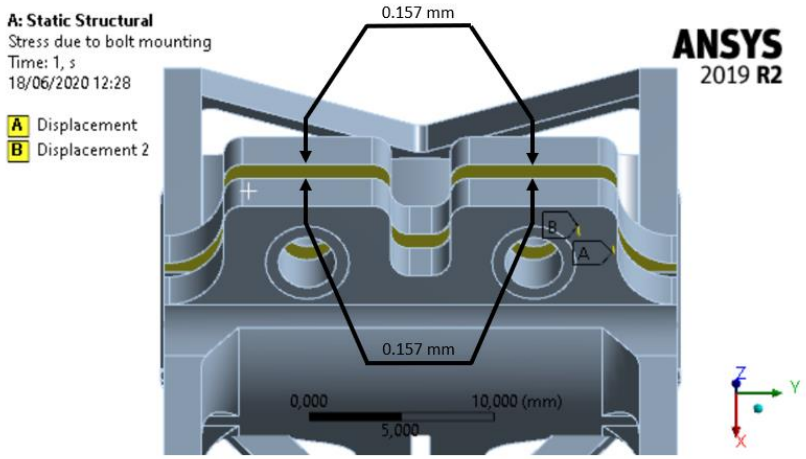

Figure 93. Displacements input applied to the bolt fixations (yellow surfaces).

Measuring the displacement on the point where the CCM center is, it is found to be of 0.36 mm, at each mirror. This value is very high since the allowed value for the interferometer to properly work is at maximum 1 micrometer.

5 Final discussion and conclusion

The results from this work show that 3d printing can effectively reduce the mass of the optical supports of the CCM (pendulum arms) of the MIMA interferometer. More than sixty different designs were tested, using diverse design methods, therefore, the results obtained are solid.

The first part of this work, focused on the optimization of the single arm, evidenced two possible geometries, both developed by topological optimization. Comparing with the mass of the previous pendulum design, the mass reduction is significant, from 14.60 g to 9.16 g, a 37% reduction, for the "Final_plate" model, the best of both (Table 21). This same model requires minimal or null AM supports to be manufactured, because of the few overhangs present. The first natural frequency is of 368 Hz and the maximum stress for the acceleration loading is of 146 MPa. This geometry will be manufactured and tested in the near future.

Indeed, the use of topology optimization proved essential in finding the best shapes. However, during the single pendulum arm design was seen that the optimization of the "external plate" model yielded better results than the optimization of the whole design region. Therefore, the algorithm used is not able to find global minimums, which raises the question whether there are even better shapes that were not found.

The second part, in which the double whole assembly of both pendulums is optimized, allows a mass reduction of 63%, from 70.00 g to 25.60 g with a first natural frequency of 445 Hz and maximum stress of 126 MPa. However, it is not able to attend all requisites due to the excessive displacement on the CCM when the shaft's clamping bolts are tightened (0.36 mm displacement, very high comparing with the 0.001 mm maximum acceptable value). To surpass this, some possible solutions is to add another degree of freedom at the CCM, allowing for vertical movement (and then, allowing for proper alignment) or to redesign the part considering this displacement, in a way that when the bolt is tightened, the mirror is displaced to its proper position. However, solving this is not the scope of this thesis work.

Also, the merged pendulums design has some manufacturing issues, due to excessive overhangs in whichever direction it is built. This requires more post processing, increasing time to manufacture and decreasing the dimensional accuracy, which is crucial for this structure.

Therefore, as much as the single piece for both pendulum arms configuration results in huge weight savings, it needs further development or changes to the mirror design to be used on the MIMA assembly. The single pendulum version developed in chapter 3 is a safer and more mature model. With the new single pendulum arm designed in section 3.5.7.2, this same assembly has a mass of approximately 59 g, a reduction of 15% comparing with the previous mass of 70.00 g.

It is essential that further experimental testing is carried out to validate this manufactured geometry. As evidenced in this study, metal AM presents many fabrication uncertainties such as possible presence of voids and deformed geometries. Therefore, after being manufactured, it must go through a tight inspection to find any major defect and later pass all tests required by the ESA to be suitable for the mission. If possible, acceleration testing will be done as well, to make sure it can withstand the landing loads.

References

[1] B. Saggin *et al*, "Design and testing of a miniaturized Fourier transform infrared spectrometer for Mars observation ," *CEAS 2011 Conference*, pp. 199-205, 2011. Available: http://hdl.handle.net/11311/607916.

[2] (). *Pasteur: Payload opportunities to search for life on Mars*. Available: https://www.esa.int/Science_Exploration/Human_and_Robotic_Exploration/Pasteur_Payload_opportunities_to_search_for_life_on_Mars.

[3] V. Formisano *et al*, "The Planetary Fourier Spectrometer (PFS) onboard the European Mars Express mission," *Planetary and Space Science*, vol. 53, *(10)*, pp. 963-974, 2005. Available: http://dx.doi.org/10.1016/j.pss.2004.12.006. DOI: 10.1016/j.pss.2004.12.006.

[4] G. Bellucci *et al*, "MIMA, a miniaturized fourier infrared spectrometer for mars ground exploration: Part I. concept and expected performance," in Oct 5, 2007, pp. 67441Q-8.

[5] B. Saggin *et al*, "MicroMIMA, a miniaturized spectrometer for planetary observation," in *2015 IEEE Metrology for Aerospace (MetroAeroSpace)*, 2015, .

[6] B. Saggin *et al*, "MIMA, a miniaturized infrared spectrometer for mars ground exploration: Part III. thermomechanical design," in Oct 5, 2007, pp. 67441S-10.

[7] S. Fonti *et al*, "MIMA, a miniaturized fourier spectrometer for mars ground exploration: Part II. optical design," in 2007, Available: https://doi.org/10.1117/12.737912. DOI: 10.1117/12.737912.

[8] European Space Agency, "ECSS-E-10-03: draft 2, Space Engineering Testing standard (2001)," .

[9] European Space Agency, "ExoMars Environment and Test Requirements -EXM-MS-SSR-AI-0004." .

[10] J. C. Najmon, S. Raeisi and A. Tovar, "2 - Review of additive manufacturing technologies and applications in the aerospace industry," *Additive Manufacturing for the Aerospace Industry*, pp. 7-31, 2019. Available: http://www.sciencedirect.com/science/article/pii/B9780128140628000029. DOI: https://doi.org/10.1016/B978-0-12-814062-8.00002-9.

[11] D. F. O. Braga *et al*, "Advanced design for lightweight structures: Review and prospects," *Progress in Aerospace Sciences*, vol. 69, pp. 29-39, 2014. Available:

http://www.sciencedirect.com/science/article/pii/S0376042114000426. DOI: https://doi.org/10.1016/j.paerosci.2014.03.003.

[12] F. H. Sam Froes, R. Boyer and B. Dutta, "ADDITIVE MANUFACTURING FOR AEROSPACE APPLICATIONS-PART II," *Adv Mater Processes*, vol. 175, *(6)*, pp. 18-22, 2017.

[13] J. Edgar and S. Tint, "Additive manufacturing technologies: 3D printing, rapid prototyping, and direct digital manufacturing," *Johnson Matthey Technology Review*, vol. 59, *(3)*, pp. 193-198, 2015.

[14] (06 February). *Siemens achieves breakthrough with 3D printed gas turbine blades*. Available: https://press.siemens.com/global/en/pressrelease/siemens-achieves-breakthrough-3d-printed-gas-turbine-blades.

[15] W. Tao and M. C. Leu, "Design of lattice structure for additive manufacturing," in *2016 International Symposium on Flexible Automation (ISFA)*, 2016, .

[16] D. S. Thomas and S. W. Gilbert, "Costs and cost effectiveness of additive manufacturing," *NIST Special Publication*, vol. 1176, pp. 12, 2014.

[17] A. H. Mostefa, S. Merdaci and N. Mahmoudi, "An overview of functionally graded materials «FGM»," in *International Symposium on Materials and Sustainable Development*, 2017, .

[18] J. S. Moya *et al*, "Functionally gradient ceramics by sequential slip casting," *Mater Lett*, vol. 14, *(5-6)*, pp. 333-335, 1992.

[19] S. Chakraverty and K. K. Pradhan, "Chapter 2 - Origin and Basics of Functionally Graded Structural Members," *Vibration of Functionally Graded Beams and Plates*, pp. 7-18, 2016. Available: http://www.sciencedirect.com/science/article/pii/B978012804228100002X. DOI: https://doi.org/10.1016/B978-0-12-804228-1.00002-X.

[20] D. Bourell *et al*, "Influence of the particle size distribution on surface quality and mechanical properties in AM steel parts," *Rapid Prototyping Journal*, 2011.

[21] A. A. Shapiro *et al*, "Additive manufacturing for aerospace flight applications," *J. Spacecraft Rockets*, pp. 952-959, 2016.

[22] M. Saadat, "Challenges in the assembly of large aerospace components," in *Integrated Systems, Design and Technology 2010*Anonymous 2011, .

[23] (). *Fired Up: GE Successfully Tested Its Advanced Turboprop Engine With 3D-Printed Parts*. Available: https://www.ge.com/reports/ge-fired-its-3d-printed-advanced-turboprop-engine/.

[24] (). *From Multiple to Singular – Consolidating Parts with Additive Manufacturing*. Available: http://www.leolane.com/blog/multiple-singular-consolidating-parts-additive-manufacturing/.

[25] S. H. Khajavi, J. Partanen and J. Holmström, "Additive manufacturing in the spare parts supply chain," *Comput. Ind.*, vol. 65, *(1)*, pp. 50-63, 2014.

[26] B. Dutta and F. H. S. Froes, "The additive manufacturing (AM) of titanium alloys," in *Titanium Powder Metallurgy*Anonymous 2015, .

[27] A. AB, "Case study: additive manufacturing of aerospace brackets," *Adv Mater Processes*, vol. 19, 2013.

[28] (). *Launch costs to low Earth orbit, 1980-2100* . Available: https://www.futuretimeline.net/data-trends/6.htm.

[29] T. Berglund, "Evaluation of fuel saving for an airline," 2008.

[30] W. E. Frazier, "Metal additive manufacturing: a review," *Journal of Materials Engineering and Performance*, vol. 23, *(6)*, pp. 1917-1928, 2014.

[31] T. Vilaro, C. Colin and J. Bartout, "As-fabricated and heat-treated microstructures of the Ti-6Al-4V alloy processed by selective laser melting," *Metallurgical and Materials Transactions A*, vol. 42, *(10)*, pp. 3190-3199, 2011.

[32] D. Gu, *Laser Additive Manufacturing of High-Performance Materials.* 2015.

[33] L. Yang *et al*, *Additive Manufacturing of Metals: The Technology, Materials, Design and Production.* 2017.

[34] L. E. Murr *et al*, "Microstructural architecture, microstructures, and mechanical properties for a nickel-base superalloy fabricated by electron beam melting," *Metallurgical and Materials Transactions A*, vol. 42, *(11)*, pp. 3491-3508, 2011.

[35] C. Qiu *et al*, "Fabrication of large Ti–6Al–4V structures by direct laser deposition," *J. Alloys Compounds*, vol. 629, pp. 351-361, 2015.

[36] A. A. Shapiro *et al*, "Additive manufacturing for aerospace flight applications," *J. Spacecraft Rockets*, pp. 952-959, 2016.

[37] S. Sarkar, C. S. Kumar and A. K. Nath, "Effect of different heat treatments on mechanical properties of laser sintered additive manufactured parts," *Journal of Manufacturing Science and Engineering*, vol. 139, *(11)*, 2017.

[38] S. Gorsse *et al*, "Additive manufacturing of metals: a brief review of the characteristic microstructures and properties of steels, Ti-6Al-4V and high-entropy alloys," *Science and Technology of Advanced MaTerialS,* vol. 18, *(1),* pp. 584-610, 2017.

[39] B. W. McEnerney *et al*, "Qualification methodology of AISi10Mg for spaceflight," 2016.

[40] E. G. Kendall, "Metals and Alloys for Cryogenic Applications-A Review," *Metals and Alloys for Cryogenic Applications-A Review,* 1964.

[41] (Jan 14,). *Metals and materials for low temperatures and cryogenic applications* . Available: https://www.gasparini.com/en/blog/metals-and-materials-for-low-temperatures/#:~:text=Other%20alloys%20resistant%20to%20even,resistant%20to%20%2D196%20%C2%B0C.

[42] (). *Ti6Al4V ELI-0406 powder for additive manufacturing*. Available: https://resources.renishaw.com/en/details/data-sheet-ti6al4v-eli-0406-powder-for-additive-manufacturing--94700.

[43] (). *SS 316L-0407 powder for additive manufacturing*. Available: https://resources.renishaw.com/en/details/data-sheet-ss-316l-0407-powder-for-additive-manufacturing--90802.

[44] (). *In718-0405 powder for additive manufacturing*. Available: https://resources.renishaw.com/en/details/data-sheet-in718-0405-powder-for-additive-manufacturing--94192.

[45] (). *AlSi10Mg-0403 powder for additive manufacturing*. Available: https://resources.renishaw.com/en/details/data-sheet-alsi10mg-0403-200-w-powder-for-additive-manufacturing--73121.

[46] S. Rojas-Labanda and M. Stolpe, "Benchmarking optimization solvers for structural topology optimization," *Structural and Multidisciplinary Optimization,* vol. 52, *(3),* pp. 527-547, 2015.

[47] X. Huang and M. Xie, *Evolutionary Topology Optimization of Continuum Structures: Methods and Applications.* 2010.

[48] G. I. Rozvany, M. Zhou and T. Birker, "Generalized shape optimization without homogenization," *Struct. Opt.,* vol. 4, *(3-4),* pp. 250-252, 1992.

[49] M. P. Bendsøe, "Optimal shape design as a material distribution problem," *Struct. Opt.,* vol. 1, *(4),* pp. 193-202, 1989.

[50] G. I. Rozvany, "A critical review of established methods of structural topology optimization," *Structural and Multidisciplinary Optimization,* vol. 37, *(3),* pp. 217-237, 2009.

[51] E. Tyflopoulos *et al*, "State of the art of generative design and topology optimization and potential research needs," *DS 91: Proceedings of NordDesign 2018, Linköping, Sweden, 14th-17th August 2018,* 2018.

[52] A. Dubrovskaya, K. Dongauzer and R. Faskhutdinov, "The design of lightweight gas turbine engine parts using topology optimization," in *MATEC Web of Conferences*, 2017, .

[53] I. ANSYS, "Ansys® Mechanical, Release 19,2, Help System, Mechanical User's Guide," 2019.

[54] ECSS - European Cooperation for Space Standarization, "Structural factors of safety for spaceflight hardware - ECSS-E-ST-32-10C Rev.2 Corrigendum 1," Aug, 2019.

[55] N. T. Aboulkhair *et al*, "Reducing porosity in AlSi10Mg parts processed by selective laser melting," *Additive Manufacturing,* vol. 1, pp. 77-86, 2014.

[56] A. Hussein *et al*, "Advanced lattice support structures for metal additive manufacturing," *J. Mater. Process. Technol.,* vol. 213, *(7),* pp. 1019-1026, 2013.

[57] J. Jiang, X. Xu and J. Stringer, "Support structures for additive manufacturing: a review," *Journal of Manufacturing and Materials Processing,* vol. 2, *(4),* pp. 64, 2018.

[58] I. ANSYS, "Ansys® Mechanical, Release 19,2, Help System, Meshing User's Guide," 2019.

[59] (). *How to Simulate and Design the Microstructures of Composites and Other Complex Materials*.

[60] (). *Friction and Friction Coefficients*. Available: https://www.engineeringtoolbox.com/friction-coefficients-d_778.html.

[61] (). *Bossard preload and tightening torques datasheet*. Available: https://www.bossard.com/en/assembly-technology-expert/technical-information-and-tools/technical-resources/preload-and-tightening-torques/.